

1      **Turbulence Measurements from Compliant Moorings - Part II: Motion**

2      **Correction**

3      Levi F. Kilcher\*

4      *National Renewable Energy Laboratory, Golden, Colorado, USA*

5      Jim Thomson

6      *Applied Physics Laboratory, University of Washington, Seattle, Washington, USA*

7      Samuel Harding

8      *Pacific Northwest National Laboratory, Richland, Washington, USA*

9      Sven Nylund

10     *Nortek AS, Norway*

11     \*Corresponding author address: Levi Kilcher, National Renewable Energy Laboratory, 15013 Den-  
12     ver West Pkwy, Golden, Colorado, USA

13     E-mail: Levi.Kilcher@nrel.gov

## ABSTRACT

Acoustic Doppler velocimeters (ADVs) are a valuable tool for making high-precision measurements of turbulence, and moorings are a convenient and ubiquitous platform for making many kinds of measurements in the ocean. However, because of concerns that mooring motion can contaminate turbulence measurements and acoustic Doppler profilers are relatively easy to deploy, ADVs are not frequently deployed from moorings. This work demonstrates that inertial motion measurements can be used to reduce motion-contamination from moored ADV velocity measurements. Three distinct mooring platforms were deployed in a tidal channel with inertial-motion-sensor-equipped ADVs. In each case, the motion correction based on the inertial measurements dramatically reduced contamination from mooring motion. The spectra from these measurements have a shape that is consistent with other measurements in tidal channels, and have a  $f^{-5/3}$  slope at high frequencies—consistent with Kolmogorov's theory of isotropic turbulence. Motion correction also improves estimates of cross spectra and Reynold's stresses. Comparison of turbulence dissipation with flow speed and turbulence production indicates a bottom boundary layer production-dissipation balance during ebb and flood that is consistent with the strong tidal forcing at the site. These results indicate that inertial-motion-sensor-equipped ADVs are a valuable new tool for measuring turbulence from moorings.

<sup>34</sup> **1. Introduction**

<sup>35</sup> Acoustic Doppler velocimeters (ADVs) have been used to make high-precision  
<sup>36</sup> measurements of water velocity for over 20 years (Kraus et al. 1994; Lohrmann  
<sup>37</sup> et al. 1995). During that time, they have been deployed around the world to  
<sup>38</sup> measure turbulence from a range of platforms, including the laboratory setting  
<sup>39</sup> (Voulgaris and Trowbridge 1998), from stationary structures on ocean-, river- and lake-bottoms  
<sup>40</sup> (Kim et al. 2000; Lorke 2007; Cartwright et al. 2009), in surface waters from a pole lowered from  
<sup>41</sup> a ship's bow (Geyer et al. 2008), and in the deep ocean from autonomous underwater vehicles  
<sup>42</sup> (e.g., Voulgaris and Trowbridge 1998; Zhang et al. 2001; Kim et al. 2000; Goodman et al. 2006; Lorke 2007)

<sup>43</sup> A relatively small fraction of ADV measurements have been made from moorings (e.g., Fer  
<sup>44</sup> and Paskyabi 2014). Presumably this is because mooring motion can contaminate ADV mea-  
<sup>45</sup> surements, and acoustic Doppler profilers (ADPs) can be used to measure mid-depth turbulence  
<sup>46</sup> statistics without a mooring (e.g., Stacey et al. 1999a; Rippeth et al. 2002; Wiles et al. 2006).  
<sup>47</sup> Still, ADV measurements have distinct characteristics that can be advantageous: they are capa-  
<sup>48</sup> ble of higher sample rates, have higher signal-to-noise ratios, and have a much smaller sample  
<sup>49</sup> volume (1 centimeter, as opposed to several meters). That is, compared to an ADP, ADVs are  
<sup>50</sup> high-precision instruments capable of providing unique information. They could be more widely  
<sup>51</sup> used as a moored instrument (i.e., at an arbitrary depth) if a method for accounting for mooring  
<sup>52</sup> motion can be demonstrated to provide more accurate estimates of turbulence statistics.

<sup>53</sup> Inertial motion unit (IMU) sensors have been used in the aerospace and aeronautical indus-  
<sup>54</sup> tries to quantify the motion of a wide range of systems, and to improve atmospheric velocity  
<sup>55</sup> measurements, for several decades (Axford 1968; Edson et al. 1998; Bevly 2004). Over the last  
<sup>56</sup> 10 years, the smartphone, drone, and ‘Internet of Things’ markets ~~has~~have driven innovation in

57 microelectrical-mechanical systems, including the IMU. As a result of this growth and innovation,  
58 the cost, power requirements, and size of IMUs have come down. These changes have allowed  
59 these sensors to be integrated into oceanographic instruments that have small form-factors, and  
60 rely on battery power.

61 Nortek now offers a version of their Vector ADV with a Microstrain 3DM-GX3-25 IMU sensor  
62 (Nortek 2005; MicroStrain 2012). This IMU's signals are incorporated into the Vector data stream,  
63 so that its motion and orientation signals are tightly synchronized with the ADV's velocity mea-  
64 surements. This tight synchronization provides a data stream that can be utilized to quantify ADV  
65 motion in the Earth's inertial reference frame, and remove that motion from the ADV's velocity  
66 measurements at each time step of its sampling (Edson et al. 1998). This work utilizes moored  
67 'ADV-IMU' measurements from mid-depths in Puget Sound to demonstrate that motion correc-  
68 tion can improve the accuracy of oceanic turbulence spectra, turbulence dissipation, and Reynolds  
69 stress estimates from moored platforms.

70 This effort was originally motivated by a need for low-cost, high-precision turbulence  
71 measurements for the emerging tidal energy industry (McCaffrey et al. 2015; Alexander and  
72 Hamlington 2015). Experience in the wind energy industry has shown that wind turbine  
73 lifetime is reduced by atmospheric turbulence, and the same is expected to be true for tidal  
74 energy turbines. In ~~wind~~ the atmosphere, meteorological towers are often used to position  
75 sonic anemometers at the hub height of wind turbines for measuring detailed turbulence inflow  
76 statistics (Hand et al. 2003; Kelley et al. 2005; Mücke et al. 2011; Afgan et al. 2013). In  
77 the ocean, tower-mounted hub-height turbulence measurements have been made, but they are  
78 challenging to install and maintain in energetic tidal sites (Gunawan et al. 2014; Thomson  
79 et al. 2012). Therefore, the U.S. Department of Energy funded this work to investigate the  
80 accuracy of mooring-deployed ADV-IMUs to reduce the cost of turbulence measurements at

81 tidal energy sites (Kilcher et al. 2016). The approach proved to be successful and potentially  
82 useful to the broader oceanographic community interested in moored turbulence measurements  
83 (Lueck and Huang 1999; Doherty et al. 1999; Nash et al. 2004; Meum and Nash 2009; Alford 2010; Paskyay  
84

The next section describes details of the measurements, including a summary of the hardware  
85 configurations (platforms) that were used to support and position the ADV-IMUs in the water  
86 column. A detailed description of the motion of these platforms is found in the companion paper to  
87 this work, Harding et al. (in review), hereafter Part 1. Section 3 describes the mathematical details  
88 of motion correction and Section 4 presents results from applying the method to measurements  
89 from the various platforms. Section 5 is a discussion of the energetics of the tidal channel in  
90 which the measurements were made and demonstrates that the measurements are consistent with  
91 turbulence theory and other measurements in similar regimes. A summary and concluding remarks  
92 are provided in Section 6.

## 93 **2. Measurements**

94 This work focuses on measuring turbulence from ADVs that are equipped with IMUs and de-  
95 ployed from moving (moored) platforms. The ADVs utilized for these measurements were Nortek  
96 Vector ADVs equipped with Microstrain 3DM-GX3-25 IMU sensors. These IMUs captured all  
97 six components of the ADV motion (three components of angular rotation and three components  
98 of linear acceleration), as well as the orientation of the ADV pressure case. The sampling of the  
99 motion sensor is tightly synchronized with the ADV measurements. The IMU measures its mo-  
100 tion at 1 kHz and uses internal signal integration (Kalman filtering) to output the motion signals  
101 at the same sample rate as the ADV's velocity measurements. This reduces aliasing of the IMU's  
102 motion measurements above the ADV's sample rate (MicroStrain 2010). Cable-head ADVs were

<sup>103</sup> used throughout this work to allow for flexibility in the positioning of the ADV head relative to its  
<sup>104</sup> pressure case.

<sup>105</sup> All measurements used in this work were made in Admiralty Inlet, Washington, approximately  
<sup>106</sup> 500 m west southwest of Admiralty Head in ~~60-m~~60 m of water near  $48^{\circ} 9.18' \text{ N}$ ,  $122^{\circ} 41.22' \text{ W}$  (Figure 1). The site is approximately 6 km east of Port Townsend, and 1 km north of the Port  
<sup>107</sup> Townsend to Coupeville ferry route. Admiralty inlet is the largest waterway connecting Puget  
<sup>108</sup> Sound to the Strait of Juan de Fuca, and it possesses a large semidiurnal tidal flow (Thomson  
<sup>109</sup> et al. 2012; Polagye and Thomson 2013). This work utilizes data from three distinct deployment  
<sup>110</sup> platforms: the tidal turbulence mooring, a StableMoor buoy, and a simple sounding weight. All  
<sup>111</sup> data used in this analysis ~~is-are~~ available from the MHK data repository (<http://mhkdr.openei.org>;  
<sup>112</sup> submission ids: 49, 50 and 51). Each of these platforms are briefly described below, and additional  
<sup>113</sup> details, photos, and schematic diagrams can be found in Part 1.  
<sup>114</sup>

<sup>115</sup> *a. Tidal Turbulence Mooring*

<sup>116</sup> The tidal turbulence mooring (TTM) is a simple mooring system with a strongback fin sus-  
<sup>117</sup> pended between a steel clump-weight anchor weighing 1,200 kg when dry and a 0.93-m-diameter  
<sup>118</sup> spherical steel buoy with a buoyancy of 320 kg. The ADV pressure cases were clamped to one  
<sup>119</sup> side of the strongback fin and the ADV sensor head was positioned 10 cm in front of the fin's  
<sup>120</sup> leading edge (Figure 2). The leading edge of the fin is fastened inline with the mooring line. This  
<sup>121</sup> configuration was designed to work like a weather vane, such that the drag on the fin held the ADV  
<sup>122</sup> head upstream of the mooring components. This work utilizes data from two TTM deployments.

<sup>123</sup> 1) ~~JUNE 2012 TTM DEPLOYMENT~~

<sup>124</sup> The first TTM deployment was in June 2012 from 17:30 on the 12th until 14:30 on the 14th  
<sup>125</sup> (local; i.e., Pacific Daylight Time). Two Nortek ADVs were clamped to either side of the fin so that  
<sup>126</sup> the axis of their cylindrical pressure cases were parallel with the leading edge of the strongback.  
<sup>127</sup> The ADV heads were spaced 0.5 m apart vertically along the fin. Only one of these ADVs was  
<sup>128</sup> equipped with an integrated IMU. This TTM also had an upward-looking acoustic Doppler profiler  
<sup>129</sup> mounted on the mooring anchor.

<sup>130</sup> Periods of time during which this mooring interfered with a beam of the Doppler profiler were  
<sup>131</sup> identified by inspecting the profiler's acoustic amplitude signal. Periods during which one beam  
<sup>132</sup> of the profiler had  $> 5\%$  higher acoustic amplitude than the other beams were flagged as "contam-  
<sup>133</sup> inated" and excluded from averaging. Five-minute averages in which more than 50% of the data  
<sup>134</sup> were contaminated in this way were masked as invalid.

<sup>135</sup> 1) ~~JUNE 2014 TTM DEPLOYMENT~~

<sup>136</sup> The second TTM deployment was in 2014 from 06:00 on June 17 to 05:00 on June 19 (local  
<sup>137</sup> time). Two Nortek ADV-IMUs were mounted on this TTM, with their heads spaced 0.5 m apart  
<sup>138</sup> along the fin. In this case, the pressure cases and ADV heads were inclined at an angle of 18° to  
<sup>139</sup> the leading edge of the fin to account for mooring blowdown during strong currents (Figure 3).  
<sup>140</sup> This change was made to reduce vibrational motion observed during the June 2012 deployment  
<sup>141</sup> that was believed to be associated with the orientation of the pressure cases.

<sup>142</sup> b. *The StableMoor platform*

<sup>143</sup> The second deployment platform was a cylindrical, StableMoor, syntactic foam buoy (manufac-  
<sup>144</sup> turer: Deep Water Buoyancy) that was anchored to a clump weight that weighed ~~2,700 lbs~~1,200

<sup>145</sup> kg (Figure 4). The buoy is 3.5 m long and 0.45 m in diameter with a tail ring that is 0.76 m in  
<sup>146</sup> diameter. The StableMoor buoy weighs 295 kg in air, and has a buoyancy of 185 kg in water.

<sup>147</sup> The StableMoor buoy was deployed with an ADV-IMU mounted at its nose from 11:21 on May  
<sup>148</sup> 12 to 11:53 on May 13, 2015 (local time). The sample volume of the ADV is 10 cm forward of  
<sup>149</sup> the nose and 20 cm above the center line of the StableMoor buoy (Figure 4). Based on Wyngaard  
<sup>150</sup> et al.'s (1985) investigation of a similarly shaped slender body, the velocity measurements should  
<sup>151</sup> have flow-distortion effects of less than 10%. This configuration was designed to be the most  
<sup>152</sup> stable platform for measuring turbulence from a moving platform. The StableMoor buoy was  
<sup>153</sup> equipped with a 1,200-kHz RDI workhorse sentinel acoustic Doppler profiler that was oriented  
<sup>154</sup> downward-looking to measure water velocity below the platform in twelve 1-m bins and measure  
<sup>155</sup> buoy motion ("bottom tracking"), all at a 1-Hz sample rate.

<sup>156</sup> The buoy was ballasted to pitch upward a few degrees in zero-flow to avoid "flying downward."  
<sup>157</sup> In the presence of an oncoming current, the tail fins help to orient it into the flow. The anchor  
<sup>158</sup> for this buoy is similar to that of the TTM, including an acoustic release so the mooring and anchor  
<sup>159</sup> can be recovered separately.

<sup>160</sup> The StableMoor platform has two primary advantages compared to the TTM. First, it is signif-  
<sup>161</sup> icantly more massive and hydrodynamically stable than the TTM, which reduces the frequency  
<sup>162</sup> of motions of the platform. Second, the StableMoor platform is capable of supporting a bottom-  
<sup>163</sup> tracking acoustic Doppler profiler, which provides an independent measure of the platform's trans-  
<sup>164</sup> lational motion. Disadvantages of the StableMoor include: its size, which adds to the challenge of  
<sup>165</sup> deployment and recovery, and its cost, which is significantly higher than the TTM system.

166 c. *Turbulence Torpedo*

167 The turbulence torpedo is a simple sounding weight with an ADV head mounted forward of the  
168 nose, and the ADV pressure case strapped below ([Figure 5](#)). This platform was deployed on May  
169 14, 2015, for 37 minutes starting at 07:41 local time. This measurement was made from a davit  
170 that hung the system from the side of the ship to a depth of approximately 25 m. The primary  
171 logistical advantages of this platform are its compact size, low cost, and the flexibility to perform  
172 spatial transects.

173 d. *Coordinate system and turbulence averaging*

174 Unless stated otherwise, vector quantities in this work are in a fixed “principal-axes” coordinate  
175 system that is aligned with the bidirectional tidal flow: positive  $u$  is in the direction of ebb (310°  
176 True), positive  $w$  is vertically upward, and  $v$  is the cross-stream component in a right-handed  
177 coordinate system. The full velocity vector,  $\vec{\tilde{u}} = (\tilde{u}, \tilde{v}, \tilde{w})$ , is separated into a mean and turbulent  
178 component as  $\vec{\tilde{u}} = \vec{\bar{u}} + \vec{u}$ , where the over-bar denotes a 5-minute average. Turbulence kinetic  
179 energy,  $tke = \overline{u^2} + \overline{v^2} + \overline{w^2}$ , and Reynold’s stresses,  $\overline{uv}$ ,  $\overline{uw}$ ,  $\overline{vw}$ , are computed by averaging over the  
180 5-minute window. Throughout this work, we use  $\bar{U} = (\bar{u}^2 + \bar{v}^2)^{1/2}$  to denote the mean horizontal  
181 velocity magnitude.

182 All spectra,  $S\{x\}(f) = |\mathcal{F}\{x(t)\}|^2$ , and cross spectra,  $C\{x,y\}(f) = \text{real}(\mathcal{F}\{x(t)\}\mathcal{F}\{y(t)\})$ , are  
183 computed using NumPy fast Fourier transform routines (van der Walt et al. 2011). Here,  $\mathcal{F}\{x(t)\}$   
184 denotes the fast Fourier transform of a signal  $x(t)$ . Time series, e.g.,  $x(t)$ , are linearly detrended  
185 and Hanning windowed prior to computing  $\mathcal{F}\{x\}$  to reduce spectral reddening.

186 Throughout the remainder of this work, the dependence of  $S$  and  $C$  on  $f$  is implied (e.g.,  $S\{x\}(f)$   
187 is hereafter  $S\{x\}$ ), and for other variables the dependence on  $t$  is implied. Spectra and cross spectra  
188 are normalized to preserve variance: ~~e.g.~~  $\int S\{u\}df = \overline{u^2}$ , and  $\int C\{u,v\}df = \overline{uv}$ . The notations

<sup>189</sup>  $S\{\vec{u}\} = (S\{u\}, S\{v\}, S\{w\})$ , and  $C\{\vec{u}\} = (C\{u, v\}, C\{u, w\}, C\{v, w\})$  denote the set of spectra and  
<sup>190</sup> cross spectra for each velocity component and pairs of components, respectively.

<sup>191</sup> Turbulence dissipation rates are computed as:

$$\epsilon = \frac{1}{\bar{U}} \left( \alpha \left\langle (S\{u\} + S\{v\} + S\{w\}) f^{5/3} \right\rangle_{f_{IS}} \right)^{3/2} \quad (1)$$

<sup>192</sup> Where ~~where~~  $\alpha = 0.5$  ~~-~~ and  $\langle \rangle_{f_{IS}}$  denotes an average over the inertial subrange of the velocity  
<sup>193</sup> spectra and where the signal-to-noise ratio is small (Lumley and Terray 1983; Sreenivasan 1995).  
<sup>194</sup> Throughout this work, we take this average from 0.3 to 1 Hz for the  $u$  and  $v$  components, and 0.3  
<sup>195</sup> to 3 Hz for the  $w$  component.

### <sup>196</sup> 3. Methodology

<sup>197</sup> ~~The essential approach of motion correction is to measure velocity on a moving platform and~~  
<sup>198</sup> ~~make an independent measurement of the platform motion, then subtract~~ This work describes  
<sup>199</sup> ~~a method for correcting velocity measurements from a moving velocity sensor,  $\vec{u}_m$ , using~~  
<sup>200</sup> ~~independent measurements of that sensor's motion,  $\vec{u}_h$ , to remove the motion from the velocity~~  
<sup>201</sup> ~~measurements, and thus estimate the 'motion corrected velocity':~~

$$\vec{u}(t) = \vec{u}_m(t) + \vec{u}_h(t) \quad . \quad (2)$$

<sup>202</sup> Note here that the '+'-sign is correct because head motion,  $\vec{u}_h$ , induces a measured velocity in the  
<sup>203</sup> opposite direction of the head motion itself ( $\vec{u}_m = \vec{u} - \vec{u}_h$ ). This approach has been used to success-  
<sup>204</sup> fully correct sonic anemometer measurements of atmospheric turbulence (e.g., Edson et al. 1998;  
<sup>205</sup> Miller et al. 2008). In the ocean, previous works have utilized inertial motion sensors to quantify  
<sup>206</sup> the motion of multiscale profilers for the purpose of measuring the full spectrum of oceanic shear  
<sup>207</sup> (Winkel et al. 1996), ~~and to quantify the motion of thermistor sensors (Moum and Nash 2009), but~~  
<sup>208</sup> ~~the Edson et al. (1998) approach has not been documented for moored ADV measurements.~~

209 Nortek's ADV-IMU The Microstrain IMU available in the Nortek Vector ADV measures the  
 210 linear acceleration,  $\vec{a}$ , rotational motion,  $\vec{\omega}$ , and orientation matrix,  $\mathbf{R}$ , of the ADV pressure case  
 211 (body) in the Earth reference frame. The Microstrain IMU integrated into the Nortek Vector ADV  
 212 has been configured to provide estimates of the ADV's orientation and motion at every time step of  
 213 the ADV's sampling (the time synchronization is  $O(10^{-2} \text{ s})$ ). So long as the ADV head is rigidly  
 214 connected to the IMU (i.e. the ADV pressure case), the motion of the ADV head is calculated  
 215 from these signals as the sum of rotational and translational motion:

$$\begin{aligned}
 \vec{u}_h &= \vec{u}_\omega + \vec{u}_a + \vec{u}_{\text{low}} \\
 &= \mathbf{R}^T \cdot \vec{\omega}^*(t) \times \vec{\ell}^* + \int \{\vec{a}(t)\}_{HP(f_a)} dt + \vec{u}_{\text{low}}
 \end{aligned} \tag{3}$$

216 Here, \* superscripts denote quantities in the ADV's local coordinate system, and  $\vec{\ell}^*$  is the vec-  
 217 tor from the IMU to the ADV head.  $\mathbf{R}^T$ —the inverse of the orientation matrix—rotates vectors  
 218 from the IMU to the Earth reference frame. The notation  $\{\vec{a}\}_{HP(f_a)}$  indicates that the IMU's  
 219 accelerometer signal is high-pass filtered (in the Earth's stationary reference frame) at a chosen  
 220 filter frequency,  $f_a$ . This is necessary because accelerometers have Without such  
 221 filtering, low-frequency noise, sometimes in  $\vec{a}$ —sometimes referred to as bias drift bias drift—is  
 222 amplified by integration to the point that it overwhelms the higher frequency information (Bar-  
 223 shan and Durrant-Whyte 1995; Bevly 2004; Gulmammadov 2009).  $\vec{u}_{\text{low}}$  is the low-frequency  
 224 translational motion that is unresolved by  $\vec{u}_a$ , and it is discussed in more detail below. Note  
 225 that, to avoid double counting,  $\vec{u}_{\text{low}}$  should be estimated by applying the complementary low-pass  
 226 filter to the independent measurement of low-frequency motion. We use fourth order, zero-phase  
 227 (bidirectional), Hanning filters for all filtering operations.

228 Integrating  $\vec{a}$  to estimate

229 The noise levels of the IMU,  $\vec{n}_\omega$  and  $\vec{n}_a$ , are computed from ADV-IMU data collected while the  
 230 instrument was resting motionless on a table for several hours. Where, for this motionless dataset,

231 the noise levels are defined according to (3) with  $\vec{n}_\omega$  in place of  $\vec{\tilde{u}}_\omega$ , and  $\vec{n}_a$  in place of  $\vec{\tilde{u}}_a$  amplifies  
232 the bias-drift noise at low frequencies, which dramatically reduces the . These are presented in  
233 Figure 6 relative to the ADV spectra presented in following sections of this paper (grey shading),  
234 and relative to the Doppler noise levels of the ADV.

235  $S\{\vec{n}_\omega\}$  is equal in all three components, and so only one component is presented for simplicity  
236 (yellow).  $S\{\vec{n}_\omega\}$  is several orders of magnitude lower than the velocity spectra we measured  
237 (grey region), and also more than an order of magnitude smaller than the Doppler noise levels of  
238 the ADV. Here we have used  $\ell^* = 1$  m; which is the order-of-magnitude of the typical distance  
239 between the ADV head and the IMU. This indicates that the precision of  $\vec{\tilde{u}}_\omega$  (i.e. the angular rate  
240 sensor) is adequate for making corrections to ADV velocity measurements without filtering.

241 The noise level of  $S\{\vec{\tilde{u}}_a\}$  (Figure 6, black), on the other hand, is dominated by a  $f^{-2}$  slope  
242 that results from integrating the low-frequency noise in  $\vec{a}$ . The horizontal ( $u$  and  $v$ ) spectra  
243 of these noise levels are identical, and so we only present one of them for simplicity (solid  
244 lines). The vertical spectra noise levels are different because the signal-to-noise ratio at those  
245 time scales (Figure ??). The high-pass filtering reduces this noise ratio is larger (dashed black  
246 lines). High-pass filtering reduces the low-frequency noise (purple and green) so that it does not  
247 contaminate motion correction, but any real motion that exists does exist at these frequencies  
248 is still lost in the low signal-to-noise ratio lost (Egeland 2014; VanZwieten et al. 2015). This  
249 means that low-frequency motion is not well resolved by the IMU, and so there is a residual low-  
250 frequency translational motion,  $\vec{\tilde{u}}_{low}$ , that needs to be measured independently—or at the very least  
251 considered—when using motion-corrected ADV-IMU data . The  $\vec{\omega}$  and  $\vec{\tilde{u}}_\omega$  estimates do not have  
252 the same issue because there is no integration involved, and because low-frequency bias-drift in  
253 the  $\vec{\omega}$  sensors is stabilized by the IMU’s on-board Kalman filtering (i.e., the accelerometer and  
254 magnetometer signals provide estimates of down and northfrom moving platforms).

255 For the StableMoor buoy, the ADP bottom-track measured  $\vec{u}_{\text{low}}$ , and this measurement agrees  
256 with  $\vec{u}_a$  over a narrow frequency band (see Part I, appendix A), indicating that the ADP and IMU  
257 are resolving the same motion. When this is the case, it is trivial to select a frequency in the middle  
258 of the spectral overlap (in this case, we choose  $f_a = 0.2$  Hz), and high-pass and low-pass filter  
259  $\vec{u}_a$  and  $\vec{u}_{\text{low}}$ , respectively, which stabilize orientation estimates and eliminates bias from rotation  
260 estimates).—then sum to estimate total translational motion. This process gives a noteworthy  
261 improvement in the shape of  $S\{u\}$  and  $S\{v\}$  for the StableMoor buoy when compared to assuming  
262  $\vec{u}_{\text{low}} = 0$  (not shown). This indicates that ADP bottom-track measurements are important for  
263 resolving turbulence spectra from the StableMoor buoy platform.

264 The choice of a high-pass filter for reducing low-frequency accelerometer noise depends on the  
265 flow conditions of the measurement and the platform being used. In particular, filter selection  
266 involves a trade-off between filtering out the bias-drift noise while not filtering out measured  
267 motion that is unresolved by an independent measurement of The position of the TTM ADV can  
268 be estimated, relative to its base, by assuming the mooring acts like a rigid pole and using the IMU  
269 orientation matrix to estimate the pole's 'lean'. The position obtained from this model can then be  
270 differentiated to estimate  $\vec{u}_{\text{low}}$ . Note that, to avoid double counting, (this model does not apply at  
271 high frequencies). Spectra of  $\vec{u}_{\text{low}}$  should be estimated by applying the complementary low-pass  
272 filter to the independent measurement of low-frequency motion estimated using this approach for  
273 the June 2014 TTM deployment (Figure 6, blue) are plotted up to the point where they cross their  
274 respective  $S\{\vec{u}_a\}$  noise level (black). Together, these two lines provide an 'aggregate noise level' of  
275 translational velocity estimates for the TTM: the rigid pole estimate of  $\vec{u}_{\text{low}}$  indicates the amplitude  
276 of unresolved motion at low- $f$  (blue), and  $S\{\vec{u}_a\}$  indicates the limits of the IMU at high- $f$  (black).  
277 Coincidentally,  $S\{\vec{u}_a\}$  filtered at  $f_a = 0.0333\text{Hz}$  is not a terrible approximation for this aggregate  
278 noise level. Furthermore, because this aggregate noise level is more than an order of magnitude

lower than the velocity spectra of interest (shaded region), the results of motion correction are essentially identical whether we use the rigid pole model to estimate  $\vec{u}_{\text{low}}$ , or if we simply assume that  $\vec{u}_{\text{low}} = 0$ .

With this estimate of ADV head motion, it is straightforward to correct the measured velocity,  $\vec{u}_m$ , to estimate the velocity in the Earth's inertial reference frame:

$$\vec{u}(t) = \vec{u}_m(t) + \vec{u}_h(t).$$

Note here that the '+' sign is correct because head motion,

The choice of  $f_a$  does influence the effectiveness of motion correction (Figure 7). When  $f_a$  is too high (e.g., 0.33 Hz, red), the high-pass filter removes resolved motion from  $\vec{u}_h$ , induces a measured velocity in the opposite direction of the head motion itself ( $\vec{u}_m = \vec{u} - \vec{u}_h$ ) that could be used to correct velocity measurements. In particular, notice that the amplitude of the 0.15 Hz peak—which is clearly the result of motion contamination (grey line)—is reduced significantly when we preserve more  $\vec{u}_h$  information by reducing the high pass filter frequency to  $f_a = 0.033$  Hz. Further reducing  $f_a$  to 0.0033 Hz does not reduce the peak further, but does increase the amplitude of the spectra at low-frequency. This low- $f$  increase is the IMU-accelerometer's low-frequency bias drift (Figure 6) returning to contaminate the motion correction method.

For the TTM and turbulence torpedo, we utilize  $f_a = 0.0333$  Hz (30-s period) and assume that  $\vec{u}_{\text{low}} = 0$ . For the StableMoor buoy,  $f_a = 0.2$  Hz (5-s period). The bottom-track velocity was low-pass filtered at this frequency to provide an estimate. Based on the above, we conclude that  $f_a = 0.033$  Hz is a convenient ‘middle’ frequency that reduces accelerometer bias-drift without destroying resolved motion of the TTM. The same  $f_a = 0.033$  Hz filter was selected, based on a similar analysis, for the turbulence torpedo. The reader is likely to notice that the 0.15 Hz peak is

300 not completely removed by motion correction, especially for the  $v$  component (Figure 7, middle  
301 panel). We will discuss this ‘persistent motion contamination’ further in the following section.  
302 Thus, we find that filter selection involves a trade-off between filtering out the bias drift noise  
303 at low-frequencies while not filtering out measured motion at high frequencies. In general, this  
304 will depend on the dynamics of the platform used to support the ADV, and the intensity of the  
305 turbulence being measured. When an independent measurement of  $\vec{u}_{\text{low}}$ , and  $\vec{a}$  was high-pass  
306 filtered at this frequency. We use 4-pole, bidirectional (zero-phase), Hanning filters for all filtering  
307 operations.

308 Spectra of  $\vec{u}_w$  (yellow) and  $\vec{u}_a$  signals from the Microstrain IMU sitting on a motionless table.  
309 The  $\vec{u}_a$  signals are unfiltered (black), and high-pass filtered at 30 s (magenta), 10 s (blue), 5  
310 s (green). Vertical dotted lines indicate the filter frequency. The black horizontal dotted line  
311 indicates the noise level of a Nortek Vector ADV configured to measure  $\pm 4 \text{ m/s}$ . The shaded  
312 region indicates the range of spectra presented herein ( $0.002 < \text{tke} < 0.03 \text{ m}^2/\text{s}^2$ ,  $1 \times 10^{-5} < \epsilon < 5 \times 10^{-4}$   
313  $\text{W/kg}$ ). is available the cross-coherence with  $\vec{u}_a$  can indicate a region of spectral overlap, and  $f_a$   
314 can be selected at the midpoint. Lacking a reliable estimate of  $\vec{u}_{\text{low}}$ , the value of  $f_a$  that produces  
315 the lowest tke estimates is likely the best.

316 Additional details on motion correction—including a detailed accounting of the distinct co-  
317 ordinate systems of the IMU, ADV pressure case, and ADV head—can be found in Kilcher  
318 et al. (2016). Open-source Python tools for performing motion correction of ADV-IMU data—  
319 including scripts that write processed data in Matlab and tabulated formats—are available at  
320 <http://lkilcher.github.io/dolfyn/>.

321 **4. Results**

322 *a. Mean velocity*

323 Figure 8 shows a comparison of  $\vec{u}$  measured by an ADV-IMU mounted on a TTM, to an upward-  
324 looking acoustic Doppler profiler mounted on the TTM anchor. This comparison shows excellent  
325 agreement between the ADV and Doppler profiler measurements of mean velocity. The  $\bar{u}$ ,  $\bar{v}$ , and  
326  $\bar{w}$  components have a root-mean-square error of 0.05, 0.13, and 0.03 m/s, respectively. Although  
327 it is important to note that there is some discrepancy between ADP- and ADV-measured velocities  
328 (especially in  $\bar{v}$ , which is most likely due to incomplete motion correction), the agreement between  
329 the magnitude and direction of these independent velocity measurements indicates that moored  
330 ADV-IMUs provide a reliable estimate of mean velocity in the Earth's reference frame.

331 *b. TTM spectra*

332 As discussed in detail in Part 1, the mooring motion of the TTM,  $S\{\vec{u}_h\}$ , has a peak at 0.1 to 0.2  
333 Hz from swaying of the mooring that is most likely driven by eddy shedding from the spherical  
334 buoy (Figure 9, red lines). There is also higher-frequency broadband motion that is associated  
335 with fluttering of the strongback fin around the mooring line. Both of these motions are especially  
336 energetic in the  $v$ -component spectra because this is the direction in which the TTM mooring  
337 system is most unstable. As is expected from fluid-structure interaction theory, the amplitude of  
338 these motions increases with increasing mean velocity (Morison et al. 1950).

339 The mooring motion contaminates the uncorrected ADV measurements of velocity,  $S\{\vec{u}_m\}$ ,  
340 whenever the amplitude of the motion is similar to or greater than the amplitude of the turbu-  
341 lence. Fortunately, much of this motion can be removed using the IMU's motion signals as de-  
342 tailed in Section 3. Lacking an independent measurement of turbulence velocity at this site, we

343 interpret the agreement of these spectra with turbulence theory as evidence that motion correc-  
344 tion has improved the velocity measurements. In particular, at high frequencies ( $f > 0.3$  Hz) for  
345 each mean-flow speed, the spectra decay with a  $f^{-5/3}$  slope and have equal amplitude across the  
346 velocity components. These results are consistent with Kolmogorov's (1941) theory of isotropic  
347 turbulence, and are consistent with spectral shapes of earlier measurements of turbulence in ener-  
348 getic tidal channels from stationary platforms (Walter et al. 2011; Thomson et al. 2012; McMillan  
349 et al. 2016).

350 For  $|\vec{u}| > 1.0$ , motion correction modifies the  $u$  and  $v$  component spectra at frequencies as high  
351 as 3 Hz. This outcome indicates that in order for motion correction to be effective, synchronization  
352 between the ADV and IMU needs to be within 1/3 s or better. This suggests that asynchronous  
353 approaches to motion correction may be challenging, especially considering that the clock drift of  
354 some instrumentation can be as high as a few seconds per day. By integrating the IMU data into  
355 the ADV data stream, the Nortek ADV-IMU achieves a synchronization to within 1e-2 s.

356 At low frequencies the spectra tend to become roughly constant (especially at higher flow  
357 speeds), which is also consistent with previous works. Note that the very low magnitude of  $S\{\vec{u}_h\}$   
358 at low frequencies is partially a result of filtering the IMU's accelerometer signal when calculating  
359  $\vec{u}_a$ . The true low-frequency spectrum of ADV head motion is unknown (indicated using a dashed  
360 line below  $f_a$ ). A comparison of  $S\{\vec{u}\}$  measured by the TTM to that measured by the ADP—during  
361 the June 2012 deployment—reveals agreement at low frequencies (not shown). This finding sug-  
362 gests that the assumption that  $\vec{u}_{\text{low}} = 0$  at these frequencies and at this site for this platform is  
363 justified—even if  $S\{\vec{u}_h\}$  is not as low as indicated in Figure 9.

364 As successful as motion correction is, some of the motion contamination persists in  $S\{\vec{u}\}$ . This  
365 is most notable in  $S\{v\}$  at the highest flow speeds ( $> 2.0$  m/s): a peak at 0.15 Hz is an order of  
366 magnitude larger than a spectral fit to the other frequencies would indicate. This persistent motion

367 contamination is evident to a lesser degree in  $S\{u\}$  for  $|u| > 2$  m/s, and in  $S\{v\}$  at lower flow  
368 speeds.  $S\{w\}$  appears to have no persistent motion contamination because the amplitude of the  
369 motion in this direction is much lower than for the other two components. For these measurements,  
370  $S\{w_h\}$  is so low that  $w$ -component motion correction makes only a minor correction to the spectra.

371 The amplitude of the persistent motion contamination peaks in  $S\{v\}$  at 0.15 Hz is a factor of 5  
372 to 10 times smaller than the amplitude of the ADV head motion itself. This observation suggests  
373 that the Microstrain IMU can be used to effectively correct mooring motion at 0.15 Hz when  
374 the amplitude of that motion is less than 5 times the amplitude of the real turbulence spectrum.  
375 As a result, we have chosen a value of 3 as a conservative estimate of the motion correction's  
376 effectiveness.

377 In addition to the primary benefit of correcting for mooring motion, the IMU measurements  
378 can also be used to identify and screen out persistent motion contamination. For example, one  
379 of the most common uses of turbulence spectra is for the calculation of  $\epsilon$  and tke. For these  
380 purposes, and based on the relative amplitudes of the 0.15-Hz peaks, we assume that persistent  
381 motion contamination is likely, where  $S\{\vec{u}_h\}/S\{\vec{u}\} > 3$ , and thereby exclude these regions from  
382 spectral fits.

383 In the present case, for the  $u$  and  $w$  spectra, this criteria only excludes a narrow range of frequen-  
384 cies at the 0.15-Hz motion peak for some cases. This criteria is more restrictive of the  $v$ -component  
385 spectra at high frequencies for  $\bar{U} > 1.0$  m/s, but this may be acceptable because the amplitude of  
386  $S\{v\}$  at these frequencies—i.e., in the isotropic inertial subrange—should be equal to that of  $S\{u\}$   
387 and  $S\{w\}$  (Kolmogorov 1941).

388 Agreement of the  $v$ -component spectral amplitude with that of  $u$  and  $w$  at frequencies  $> 0.3$  Hz  
389 indicates that motion correction is effective at those frequencies even when  $S\{\vec{u}_h\}/S\{\vec{u}\} \gtrsim 3$ . This  
390 outcome suggests that our screening threshold is excessively conservative at those frequencies,

391 and that a more precise screening threshold may be frequency dependent. For example, it might  
392 take into account the  $f^3$  character of the noise in  $S\{\vec{u}_a\}$  (Figure ??6). For the purpose of this  
393 work, the  $S\{\vec{u}_h\}/S\{\vec{u}\} < 3$  threshold for spectral fits is sufficient, and detailed characterization of  
394 the IMU's motion- and frequency-dependent noise level is left for future work.

395 *c. StableMoor Spectra*

396 The spectra of the StableMoor motion has a broader peak with a maximum amplitude that is ap-  
397 proximately half the frequency of the TTM spectral peak (Figure 10). The motion of this platform  
398 also does not have high-frequency “subpeaks” or other high-frequency broadband excitation  
399 (Part 1). These characteristics of the motion are most likely due to the more massive and hydro-  
400 dynamically streamlined properties of the platform.

401 Like the TTM, the motion-corrected spectra from the StableMoor buoy are consistent with turbu-  
402 lence theory and previous observations. Most importantly, there is an improvement in the quality  
403 of the motion-corrected spectra compared to the TTM. In particular, the persistent motion con-  
404 tamination peaks are completely removed. That is, this measurement system provides an accurate  
405 estimate of the turbulence spectra at this location from low frequencies to more than 1Hz—well-1  
406 Hz—well into the inertial subrange—for all three components of velocity.

407 Note that this level of accuracy cannot be obtained without the independent estimate of  $\vec{u}_{low}$ .  
408 If we assume that  $\vec{u}_{low} = 0$ , a similar plot to Figure 10 (not shown) reveals persistent motion-  
409 contamination peaks and troughs in the  $u$  and  $v$  spectra regardless of the choice of  $f_a$ . This as-  
410 sumption indicates that the low-frequency motion of the StableMoor buoy is below a threshold in  
411 which the IMU's signal-to-noise ratio is high enough to resolve its motion. In other words, com-  
412 pared to the TTM, the StableMoor platform provides a more accurate measurement of turbulence

<sup>413</sup> when it includes an independent measure of  $\vec{u}_{\text{low}}$  (here a bottom-tracking ADCP), but it does no  
<sup>414</sup> better—and perhaps worse—when it does not.

<sup>415</sup> *d. Torpedo spectra*

<sup>416</sup> The  $u$  and  $v$  motion of the turbulence torpedo is ~~broadbanded broadband~~ and the  $w$  motion has a  
<sup>417</sup> narrow peak at 0.3 Hz (Figure 11). Because  $\vec{u}_h$  is estimated using  ~~$f_a = 0.0333 \text{ Hz}$~~   $f_a = 0.0333 \text{ Hz}$   
<sup>418</sup> and assuming  $\vec{u}_{\text{low}} = 0$ , its spectra rolls off quickly below  $f_a$ . Motion correction of the torpedo  
<sup>419</sup> data appears to effectively remove a motion peak from  $S\{w\}$  at 0.3 Hz, and straightens out  $S\{v\}$   
<sup>420</sup> between 0.04 and 0.6 Hz.  $S\{u\}$  is mostly unaffected by motion at these frequencies, because the  
<sup>421</sup> torpedo motion is smaller than the turbulence in this direction. At frequencies below  $f_a$ ,  $S\{u\}$  and  
<sup>422</sup>  $S\{v\}$  increase dramatically. This increase suggests that unresolved, low-frequency motion of the  
<sup>423</sup> torpedo is contaminating the velocity measurements at these frequencies. It may be possible to  
<sup>424</sup> correct for some of this contamination using a measurement of the ship’s motion as a proxy for the  
<sup>425</sup> torpedo’s low-frequency motion, but this has not been done. Still, above  $f_a$ , the torpedo appears to  
<sup>426</sup> provide a reliable estimate of spectral amplitude in the inertial subrange and can therefore be used  
<sup>427</sup> to estimate  $\epsilon$ . Considering the simplicity of the platform, it may be a useful option for quantifying  
<sup>428</sup> this ~~essential turbulence quantity~~ turbulence statistic in a variety of scenarios. Further, if a GPS is  
<sup>429</sup> positioned above it, it may be capable of providing even more.

<sup>430</sup> *e. Cross Spectra*

<sup>431</sup> ~~Inspection of cross spectra from TTM measurements demonstrates that motion correction can~~  
<sup>432</sup> ~~reduce motion contamination to produce reliable estimates of velocity cross spectra (Figure 12). At~~  
<sup>433</sup> ~~low flow speeds (left column), cross spectra between components of  $\vec{u}_h$  (i.e., between components~~  
<sup>434</sup> ~~of head motion~~ Cross-spectra indicate the correlation between different velocity components as a

435 function of frequency, and their integrals are the Reynold's stresses. Head motion cross-spectra,  
436  $C\{\vec{u}_h\}$  (Figure 12, red), and uncorrected velocity cross-spectra, red) are small compared to  
437 correlated velocities. As the velocity magnitude increases (center and right columns), the swaying  
438 motion of the TTM at  $C\{\vec{u}_m\}$  (black), from TTM measurements have large peaks at the same  
439 frequency ( 0.15 Hzappears as a peak in ) as peaks in auto-spectra (Figure 9). This indicates  
440 that mooring motion contaminates the uncorrected cross-spectral velocity measurements, and that  
441 Reynold's stress estimates based on uncorrected velocity measurements will be contaminated by  
442 mooring motion. This makes sense because mooring swaying in a direction not aligned with one  
443 of the major principal axes will, for example, introduce spurious cross-spectra and contaminate  
444 the Reynold's stress.

445 Fortunately, motion corrected velocity cross-spectra,  $C\{\vec{u}\}$  (blue), have reduced spectral  
446 amplitudes at these frequencies (reduced peaks), which indicates that motion correction reduces  
447 motion contamination to produce more reliable estimates of velocity cross spectra and Reynold's  
448 stresses (Figure 12). In particular, the amplitude of the cross spectra of  $\vec{u}_h$  (red)uncertainty in  
449  $f \cdot C\{\vec{u}\}$  (indicated by the blue shading), is significantly smaller than the mean values of  $C\{\vec{u}_h\}$  and  
450  $\vec{u}_m$  (black)for all three components of cross spectra (rows). Fortunately, motion correetion reduces  
451 the amplitude of this peak dramatically so that  $C\{\vec{u}\}$  (blue) is small at  $C\{\vec{u}_m\}$  at the frequencies of  
452 maximum motion (0.15 Hzcompared to lower frequencies. Furthermore, the fact that the standard  
453 deviation ). This indicates that even the individual estimates of  $C\{\vec{u}\}$  is also relatively small at  
454 0.15 Hz suggests that motion correction is effective for each spectral windowhave reduced peaks  
455 at these frequencies, not just in their mean. the mean.

456 These results indicate that motion-corrected TTM velocity measurements can be used to obtain  
457 reliable estimates of turbulence Reynold's stresses, which are the integral of the cross spectra.

458 Without motion correction, Reynold's stress estimates would be contaminated by the large peaks  
459 in the cross spectra that are caused by the swaying and fluttering motion of the TTM vane.

460 A similar investigation of StableMoor cross spectra (not shown) indicates that cross-spectral  
461 motion contamination is at a much lower amplitude than for the TTM. The low-frequency (< 0.3  
462 Hz) "swimming" motion of that platform produces a minimal cross-spectral signal, and the relative  
463 large mass of the platform minimizes the kinds of higher-frequency swaying and fluttering that  
464 creates large values of cross-spectral head motion. Thus, the StableMoor platform also produces  
465 reliable estimates of Reynold's stresses, which are presumed to be improved by motion correction.

## 466 5. Discussion

467 The previous section presented a comparison of  $\vec{u}$  measured by a TTM-mounted ADV to mea-  
468 surements from a co-located ADP. This comparison demonstrated that the IMU provides a reliable  
469 estimate of the ADV's orientation and that this can be utilized to estimate mean velocity in the  
470 Earth's reference frame. Turbulence velocity estimates from the same ADP are also in agree-  
471 ment with low-frequency TTM turbulence estimates (not shown), but the ADP does not resolve  
472 turbulence at the scales where motion contamination is strongest (0.1 to 1.0 Hz).

473 Ideally, moored motion-corrected turbulence velocity measurements would be validated against  
474 simultaneous independent validated measurements of turbulence velocity at the same scales and  
475 exact time and location. Accomplishing this, however, involves significant technical challenges  
476 that are not easily overcome—most notably the difficulty of measuring turbulence at the same point  
477 as the moving ADV. A slightly less ideal but much more realistic confirmation of the methodology  
478 might involve comparing the statistics of moored turbulence measurements to those from a nearby  
479 fixed platform, or a fixed platform placed at the same location at a different time (e.g., the "TTT"

480 platform described in Thomson et al. 2012). Unfortunately, to our knowledge, these measurements  
481 have not yet been made.

482 Lacking a relevant, fixed, independent turbulence measurement to compare to it is instructive  
483 to demonstrate the degree to which the moored measurements are consistent with turbulence  
484 theory and other turbulence measurements in similar flow environments. The previous section  
485 showed that the shape of the turbulence velocity spectra from moored ADVs is consistent with  
486 Kolmogorov's theory of locally isotropic turbulence, which has been observed consistently in tur-  
487 bulence measurements for decades (Kolmogorov 1941; Grant et al. 1962; McMillan et al. 2016).  
488 In particular, we observed an isotropic subrange—an  $f^{-5/3}$  spectral slope and equal amplitude  
489 spectra between components—that is driven by anisotropic turbulence at longer timescales (Fig-  
490 ures 9, 10, 11). This finding is interpreted as the first indication that the measurement systems  
491 presented are capable of accurately resolving turbulence. The degree to which uncorrected spec-  
492 tra were corrected toward this theoretical and observationally confirmed shape is interpreted as a  
493 measure of the improvement of the spectral estimates by motion correction.

494 Figure 13 presents a time series of the mean velocity (A) and several turbulence statistics that  
495 were measured during the June 2014 TTM deployment. This figure shows the evolution of the flow  
496 through Admiralty Inlet during 1.5 tidal cycles. The tke (B), Reynold's stresses (C), dissipation,  
497 and one component of turbulence production (D) grow and strengthen with ebb or flood then  
498 subside during slack tide. This component of turbulence production is:

$$P_{uz} = \frac{\partial \bar{u}}{\partial z} \bar{u} \bar{w} \frac{\partial \bar{u}}{\partial z} . \quad (4)$$

499 Where  $\partial \bar{u} / \partial z$  is computed from the two ADVs on the TTM. The highest values of  $\epsilon$  and  $P_{uz}$  occur  
500 at the peak of the ebb or flood, which is in agreement with other measurements in tidal channels.  
501 The agreement of the magnitude of  $P_{uz}$  with  $\epsilon$  at those times suggests a local production-dissipation

balance that is often observed in tidally forced channels (Trowbridge et al. 1999; Stacey et al. 1999b; McMillan et al. 2016). At other times, the value of  $P_{uz}$  is insufficient to balance  $\varepsilon$  or is negative.

~~$P_{uz}$  vs.  $\varepsilon$  during the June 2014 TTM deployment for values of  $|u| > 1 \text{ m/s}$ . Values of negative production are indicated as open circles.~~

Inspection of the negative  $P_{uz}$  values reveals that most of them are caused by a reversed sign of  $\overline{uw}$  rather than a reversed sign of  $\partial u / \partial z$  (i.e., when compared to the sign of  $u$ ). This finding suggests that uncertainty in  $\overline{uw}$  may be contributing to discrepancies between  $P_{uz}$  and  $\varepsilon$ . Furthermore, considering the complex nature of the ~~shoreline near bathymetry and shoreline at~~ this site (i.e., the headland), it is not surprising that  $P_{uz}$  does not ~~perfectly~~ balance  $\varepsilon$ ~~perfectly~~. Other terms of the equation are likely to be important, such as ~~turbulence advection, other components of production, advection terms, or turbulent transport terms and turbulent transport~~. The fact that ~~these two—the  $P_{uz}$  and  $\varepsilon$  terms~~ are in near balance as often as they are ~~is a strong indication~~ indicates that bottom boundary layer physics are important to the ~~turbulence~~ dynamics at this site.

Figure 14 compares individual values of  $P_{uz}$  with  $\varepsilon$  directly. Given the assumptions implicit in this comparison and the discussion above, the ~~degree of~~ agreement between  $P_{uz}$  and  $\varepsilon$ ~~is an encouraging result that suggests the turbulent boundary—especially for the highest values of~~  $\varepsilon$ ~~suggests the turbulent boundary layer~~ reaches the depth of these measurements (10 m) during the highest flow speeds. This result is further supported by a comparison of  $\bar{U}$  with  $\varepsilon$  (Figure 15). Here we see a  $\varepsilon \propto \bar{U}^3$  dependence that is again suggestive of bottom boundary layer physics (Trowbridge 1992; Nash et al. 2009). At lower flow speeds,  $\varepsilon$  deviates from this relationship, which suggests that the boundary layer is no longer the dominant physical process at the depth of these measurements.

525 There are two intriguing differences between the ebb and flood datasets: 1) the drag coefficient  
526 relating  $\epsilon$  to  $\bar{U}^3$  is larger for ebbs, and 2) the fit does not hold as well for low flow speeds (Figure  
527 15). These details are not surprising considering the complex bathymetry at the test site (Figure  
528 1). In particular, the flow immediately upstream of the measurement site is exposed to much  
529 more bathymetric curvature—i.e. from the headland—during ebb (when  $\bar{u}$  is  $> 0$ ) than during  
530 flood ( $\bar{u} < 0$ ). Based on this, one might expect flow separation (turbulence advection), turbulence  
531 production, or turbulence transport emanating from the headland to have a stronger impact on  
532 the flow at this site during ebb than flood. These effects are a likely contributor to the distinct  
533 relationships observed in Figure 15.

534 The hypothesis that the headland is a key contributor to the turbulence dynamics at this site  
535 suggests that terms such as cross-stream turbulence advection,  $\bar{v}\partial tke/\partial y$ , the lateral turbulent  
536 transport terms,  $\partial\bar{u}_i u_i \bar{v}/\partial y$ , or lateral shear production,  $\bar{u}\bar{v}\partial\bar{u}/\partial y$ , may contribute significantly to  
537 the dynamics of turbulence at this site. While we did not measure stratification profiles during  
538 these measurements, we do not typically expect buoyancy flux to play dominant role due to the  
539 fact that this region tends to be tidally well-mixed (Geyer and Cannon 1982). In summary, bottom  
540 boundary layer physics seems to be the dominant process at the measurement site, with lateral  
541 advection, lateral transport, and lateral production of tke also potentially contributing—especially  
542 during ebb. A more detailed analysis of the turbulence and momentum dynamics of this headland  
543 is left for future work (e.g., Warner et al. 2013).

## 544 6. Conclusion

545 This work presents a methodology for measuring turbulence from moored ADV-IMUs and  
546 demonstrates that motion correction reduces mooring motion-contamination. Comparison of spec-  
547 tra of ADV head motion,  $S\{\vec{u}_h\}$ , to that of motion-corrected,  $S\{\vec{u}\}$ , and uncorrected spectra,

548  $S\{\vec{u}_m\}$ , reveals that motion correction improves spectral estimates of moored ADV measurements.  
549 In particular, we found that motion-corrected spectra have spectral shapes that are similar to previ-  
550 ous measurements of tidal-channel turbulence and have a  $f^{-5/3}$  spectral slope at high frequencies.  
551 This finding suggests that the motion-corrected spectra resolve the inertial subrange predicted by  
552 Kolmogorov's theory of locally isotropic turbulence.

553 Motion correction reduces motion contamination for all platforms we presented but it does not  
554 necessarily remove it completely. This outcome seems to depend on the relative amplitude of plat-  
555 form motion compared to the underlying turbulence being measured. The most notable example  
556 of this is from the TTM, ~~which has a large “swaying” peak at 0.1 Hz. Where this peak is very~~  
557 ~~large—especially in the  $v$  component—it is not reduced to a level that is consistent with earlier~~  
558 ~~measurements of tidal-channel turbulence—i.e., there is no smooth  $v$ -component spectra, which~~  
559 ~~have a large-amplitude “swaying” peak at 0.15 Hz that interrupts the often observed ‘roll-off’ be-~~  
560 ~~tween the low-frequency energy-containing scales ‘energy containing scales’ and the  $f^{-5/3}$  inertial~~  
561 ~~subrange.~~

562 This inconsistency indicates that turbulence measurements from moored, motion-corrected ~~IMU~~  
563 ~~ADVs-ADV-IMUs~~ must be interpreted with care. An inspection of spectra presented here suggests  
564 that excluding spectral regions where  $S\{\vec{u}_h\}/S\{\vec{u}\} > 3$  removes persistent-motion contamination  
565 peaks while still preserving spectral regions where motion correction is effective. Using this cri-  
566 teria, it is then possible to produce spectral fits that exclude persistent-motion contamination, and  
567 provide reliable estimates of turbulence quantities of interest (e.g.,  $\varepsilon$  and tke).

568 We ~~‘ve have~~ also shown that motion correction reduces motion contamination in cross spectra.  
569 This finding is important because it suggests that moored ~~IMU-ADV-ADV-IMU~~ measurements  
570 may be used to produce reliable estimates of Reynolds stresses. We utilized these stress estimates  
571 and vertical shear estimates, both from the TTM, to estimate  $P_{uz}$ .

572 Finally, we have shown that  $\varepsilon$  estimates based on motion-corrected spectra scale with the  $U^3$ ,  
573 and balance  $P_{uz}$  estimates during peak ebb and flood. Together, these results indicate that bottom  
574 boundary layer physics are a dominant process at this site, and that the boundary layer reaches  
575 the height of the ~~IMU-ADVs~~ADV-IMUs (10 m) during ebb and flood. The degree of agree-  
576 ment between  $P_{uz}$  and  $\varepsilon$  also serves as an indicator of the self-consistency of moored ~~IMU-ADV~~  
577 ADV-IMU turbulence measurements.

578 *Acknowledgments.* Many thanks to Joe Talbert, Alex DeKlerk, Captain Andy Reay-Ellers, Jen-  
579 nifer Rinker, Maricarmen Guerra, and Eric Nelson in assisting with data collection. The authors  
580 are also grateful to James VanZwieten, Matthew Egeland and Marshall Richmond for discussion  
581 on the details of this work.

582 Thanks to the open-source software community for the tools used in this work, especially the  
583 developers of L<sup>A</sup>T<sub>E</sub>X, Python, NumPy, Matplotlib, git, and GNU emacs.

584 This work was supported by the U.S. Department of Energy under Contract No. DE-AC36-  
585 08GO28308 with the National Renewable Energy Laboratory. Funding for the work was provided  
586 by the DOE Office of Energy Efficiency and Renewable Energy, Wind and Water Power Technolo-  
587 gies Office.

588 The U.S. Government retains and the publisher, by accepting the article for publication, ac-  
589 knowledges that the U.S. Government retains a nonexclusive, paid-up, irrevocable, worldwide  
590 license to publish or reproduce the published form of this work, or allow others to do so, for U.S.  
591 Government purposes.

592    **References**

- 593    Afgan, I., J. McNaughton, S. Rolfo, D. Apsley, T. Stallard, and P. Stansby, 2013: Turbulent flow  
594    and loading on a tidal stream turbine by les and rans. *International Journal of Heat and Fluid*  
595    *Flow*, **43**, 96–108.
- 596    Alexander, S. R., and P. E. Hamlington, 2015: Analysis of turbulent bending moments in tidal  
597    current boundary layers. *Journal of Renewable and Sustainable Energy*, **7 (6)**, 063 118.
- 598    Alford, M. H., 2010: Sustained, full-water-column observations of internal waves and mixing near  
599    mendocino escarpment. *Journal of Physical Oceanography*, **40 (12)**, 2643–2660, doi:10.1175/  
600    2010JPO4502.1.
- 601    Axford, D., 1968: On the accuracy of wind measurements using an inertial platform in an aircraft,  
602    and an example of a measurement of the vertical mesostructure of the atmosphere. *Journal of*  
603    *Applied Meteorology*, **7 (4)**, 645–666.
- 604    Barshan, B., and H. F. Durrant-Whyte, 1995: Inertial navigation systems for mobile robots. *IEEE*  
605    *Transactions on Robotics and Automation*, **11 (3)**, 328–342.
- 606    Bevly, D. M., 2004: Global positioning system (gps): A low-cost velocity sensor for correcting in-  
607    ertrial sensor errors on ground vehicles. *Journal of dynamic systems, measurement, and control*,  
608    **126 (2)**, 255–264.
- 609    Cartwright, G. M., C. T. Friedrichs, P. J. Dickhudt, T. Gass, and F. H. Farmer, 2009: Using the  
610    acoustic doppler velocimeter (adv) in the mudbed real-time observing system. *Marine Technol-  
611    ogy for Our Future: Global and Local Challenges*.
- 612    Doherty, K., D. Frye, S. Liberatore, and J. Toole, 1999: A moored profiling instrument\*. *Journal*  
613    *of Atmospheric and Oceanic Technology*, **16 (11)**, 1816–1829.

- 614 Edson, J. B., A. A. Hinton, K. E. Prada, J. E. Hare, and C. W. Fairall, 1998: Direct covariance  
615 flux estimates from mobile platforms at sea\*. *Journal of Atmospheric and Oceanic Technology*,  
616 **15** (2), 547–562, doi:10.1175/1520-0426(1998)015<0547:DCFEFM>2.0.CO;2.
- 617 Egeland, M. N., 2014: Spectral evaluation of motion compensated ADV systems for ocean turbu-  
618 lence measurements. Ph.D. thesis, Florida Atlantic University.
- 619 Fer, I., and M. B. Paskyabi, 2014: Autonomous ocean turbulence measurements using shear probes  
620 on a moored instrument. *Journal of Atmospheric and Oceanic Technology*, **31** (2), 474–490, doi:  
621 10.1175/JTECH-D-13-00096.1.
- 622 Finlayson, D., 2005: Combined bathymetry and topography of the Puget Lowlands, Washington  
623 state. URL <http://www.ocean.washington.edu/data/pugetsound/>.
- 624 Geyer, R. W., M. E. Scully, and D. K. Ralston, 2008: Quantifying vertical mixing in estuaries.  
625 *Environmental Fluid Mechanics*, **8**, 495–509, doi:10.1007/s10652-008-9107-2.
- 626 Geyer, W. R., and G. A. Cannon, 1982: Sill processes related to deep water renewal in a fjord. *Jour-*  
627 *nal of Geophysical Research: Oceans*, **87** (C10), 7985–7996, doi:10.1029/JC087iC10p07985.
- 628 Goodman, L., E. R. Levine, and R. G. Lueck, 2006: On measuring the terms of the turbulent  
629 kinetic energy budget from an auv. *Journal of Atmospheric and Oceanic Technology*, **23** (7),  
630 977–990, doi:10.1175/JTECH1889.1.
- 631 Grant, H. L., R. W. Stewart, and A. Moilliet, 1962: Turbulence spectra from a tidal channel.  
632 *Journal of Fluid Mechanics*, **12**, 241–263.
- 633 Gulmammadov, F., 2009: Analysis, modeling and compensation of bias drift in mems inertial  
634 sensors. *Recent Advances in Space Technologies, 2009. RAST'09. 4th International Conference*  
635 *on*, IEEE, 591–596.

- 636 Gunawan, B., V. S. Neary, and J. Colby, 2014: Tidal energy site resource assessment in the East  
637 River tidal strait, near Roosevelt Island, New York, NY (USA). *Renewable Energy*, **71**, 509–  
638 517, doi:10.1016/j.renene.2014.06.002.
- 639 Hand, M. M., N. D. Kelley, and M. J. Balas, 2003: Identification of wind turbine response to  
640 turbulent inflow structures. Tech. Rep. NREL/CP-500-33465, National Renewable Energy Lab-  
641 oratory.
- 642 Harding, S., L. Kilcher, and J. Thomson, 2017: Turbulence measurements from compliant moor-  
643 ings - part 1: Motion characterization, in review.
- 644 Kelley, N. D., B. J. Jonkman, G. N. Scott, J. T. Bialasiewicz, and L. S. Redmond, 2005: The impact  
645 of coherent turbulence on wind turbine aeroelastic response and its simulation. *WindPower*,  
646 Denver, Colorado, NREL/CP-500-38074, may 15-18.
- 647 Kilcher, L., J. Thomson, J. Talbert, and A. DeKlerk, 2016: Measuring turbulence from moored  
648 acoustic Doppler velocimeters: A manual to quantifying inflow at tidal energy sites. 9 62979,  
649 National Renewable Energy Laboratory. URL [www.nrel.gov/docs/fy16osti/62979.pdf](http://www.nrel.gov/docs/fy16osti/62979.pdf).
- 650 Kim, S. C., C. T. Friedrichs, J. P.-Y. Maa, and L. D. Wright, 2000: Estimating bottom stress in  
651 tidal boundary layer from acoustic doppler velocimeter data. *Journal of Hydraulic Engineering*,  
652 399–406.
- 653 Kolmogorov, A. N., 1941: Dissipation of energy in the locally isotropic turbulence. *Dokl. Akad.*  
654 *Nauk SSSR*, **32** (1), 16–18, URL <http://www.jstor.org/stable/51981>.
- 655 Kraus, N. C., A. Lohrmann, and R. Cabrera, 1994: A new acoustic meter for measuring 3D  
656 laboratory flows. *Journal of Hydraulic Engineering*, **120**, 406–412.

- 657 Lohrmann, A., R. Cabrera, G. Gelfenbaum, and J. Haines, 1995: Direct measurements of reynolds  
658 stress with an acoustic doppler velocimeter. *Current Measurement, 1995.*, *Proceedings of the*  
659 *IEEE Fifth Working Conference on*, 205–210, doi:10.1109/CCM.1995.516175.
- 660 Lorke, A., 2007: Boundary mixing in the thermocline of a large lake. *Journal of Geophysical*  
661 *Research: Oceans*, **112 (C9)**, n/a–n/a, doi:10.1029/2006JC004008, c09019.
- 662 Lueck, R. G., and D. Huang, 1999: Dissipation measurement with a moored instrument in a swift  
663 tidal channel. *Journal of atmospheric and oceanic technology*, **16**, 1499–1505.
- 664 Lumley, J., and E. Terray, 1983: Kinematics of turbulence convected by a random wave field.  
665 *Journal of Physical Oceanography*, **13 (11)**, 2000–2007.
- 666 McCaffrey, K., B. Fox-Kemper, P. E. Hamlington, and J. Thomson, 2015: Characterization of  
667 turbulence anisotropy, coherence, and intermittency at a prospective tidal energy site: Observa-  
668 tional data analysis. *Renewable Energy*, **76**, 441–453.
- 669 McMillan, J. M., A. E. Hay, R. G. Lueck, and F. Wolk, 2016: Rates of dissipation of turbulent  
670 kinetic energy in a high reynolds number tidal channel. *Journal of Atmospheric and Oceanic*  
671 *Technology*, **33 (4)**, 817–837, doi:10.1175/JTECH-D-15-0167.1.
- 672 MicroStrain, I., 2010: Technical note: Coning and sculling. Tech. Rep. I0019, MicroStrain. URL  
673 [http://files.microstrain.com/TN-I0019\\_3DM-GX3-25\\_\\_Coning\\_And\\_Sculling.pdf](http://files.microstrain.com/TN-I0019_3DM-GX3-25__Coning_And_Sculling.pdf).
- 674 MicroStrain, I., 2012: *3DM-GX3-15,-25 MIP Data Communications Protocol*. URL <http://files.microstrain.com/3DM-GX3-15-25-MIP-Data-Communications-Protocol.pdf>, retrieved  
675 January 2014.

- 677 Miller, S. D., T. S. Hristov, J. B. Edson, and C. A. Friehe, 2008: Platform motion effects on  
678 measurements of turbulence and air-sea exchange over the open ocean. *Journal of Atmospheric*  
679 *and Oceanic Technology*, **25** (9), 1683–1694, doi:10.1175/2008JTECHO547.1.
- 680 Morison, J. R., J. W. Johnson, and S. A. Schaaf, 1950: The force exerted by surface waves on  
681 piles. *Journal of Petroleum Technology*, **2** (05), 149–154.
- 682 Moum, J., and J. Nash, 2009: Mixing measurements on an equatorial ocean mooring. *Journal of*  
683 *Atmospheric and Oceanic Technology*, **26** (2), 317–336.
- 684 Mücke, T., D. Kleinhans, and J. Peinke, 2011: Atmospheric turbulence and its influence on the  
685 alternating loads on wind turbines. *Wind Energy*, **14**, 301–316.
- 686 Nash, J. D., L. F. Kilcher, and J. N. Moum, 2009: Structure and composition of a strongly  
687 stratified, tidally pulsed river plume. *Journal of Geophysical Research*, **114**, C00B12, doi:  
688 10.1029/2008JC005036.
- 689 Nash, J. D., E. Kunze, J. M. Toole, and R. W. Schmitt, 2004: Internal tide reflection and turbulent  
690 mixing on the continental slope. *Journal of Physical Oceanography*, **34** (5), 1117–1134, doi:  
691 10.1175/1520-0485(2004)034<1117:ITRATM>2.0.CO;2.
- 692 Nortek, 2005: *Vector Current Meter User Manual*. Vangkroken 2, NO-1351 RUD, Norway, h ed.
- 693 Paskyabi, M. B., and I. Fer, 2013: Turbulence measurements in shallow water from a subsurface  
694 moored moving platform. *Energy Procedia*, **35**, 307 – 316, doi:10.1016/j.egypro.2013.07.183.
- 695 Perlin, A., and J. N. Moum, 2012: Comparison of thermal variance dissipation rates from moored  
696 and profiling instruments at the equator. *Journal of Atmospheric and Oceanic Technology*.

- 697 Polagye, B., and J. Thomson, 2013: Tidal energy resource characterization: methodology and field  
698 study in admiralty inlet, Puget Sound, WA (USA). *Proceedings of the Institution of Mechanical*  
699 *Engineers, Part A: Journal of Power and Energy*, **227** (3), 352–367.
- 700 Rippeth, T. P., E. Williams, and J. H. Simpson, 2002: Reynolds stress and turbulent en-  
701 ergy production in a tidal channel. *Journal of Physical Oceanography*, **32**, 1242–1251, doi:  
702 10.1175/1520-0485(2002)032\$(\$1242:RSATEP\$)\$2.0.CO;2.
- 703 Sreenivasan, K. R., 1995: On the universality of the Kolmogorov constant. *Physics of Fluids*, **7**,  
704 2778–2784.
- 705 Stacey, M. T., S. G. Monismith, and J. R. Burau, 1999a: Measurements of reynolds stress  
706 profiles in unstratified tidal flow. *J. Geophys. Res.*, **104** (C5), 10 933–10 949, doi:10.1029/  
707 1998JC900095.
- 708 Stacey, M. T., S. G. Monismith, and J. R. Burau, 1999b: Observations of turbulence in a partially  
709 stratified estuary. *Journal of Physical Oceanography*, **29**, 1950–1970.
- 710 Thomson, J., B. Polagye, V. Durgesh, and M. Richmond, 2012: Measurements of turbulence at  
711 two tidal energy sites in Puget Sound, WA. *Journal of Oceanic Engineering*, **37** (3), 363–374,  
712 doi:10.1109/JOE.2012.2191656.
- 713 Trowbridge, J. H., 1992: A simple description of the deepening and structure of a stably stratified  
714 flow driven by a surface stress. *Journal of Geophysical Research*, **97**, 15 529–15 543.
- 715 Trowbridge, J. H., W. R. Geyer, M. M. Bowen, and A. J. I. Williams, 1999: Near-bottom turbu-  
716 lence measurements in a partially mixed estuary: turbulent energy balance, velocity structure  
717 and along-channel momentum balance. *Journal of Physical Oceanography*, **29**, 3056–3072.

- 718 van der Walt, S., S. C. Colbert, and G. Varoquaux, 2011: The numpy array: A structure for efficient  
719 numerical computation. *Computing in Science & Engineering*, **13**, 22–30, doi:10.1109/MCSE.  
720 2011.37.
- 721 VanZwieten, J. H., M. N. Egeland, K. D. von Ellenrieder, J. W. Lovenbury, and L. Kilcher, 2015:  
722 Experimental evaluation of motion compensated adv measurements for in-stream hydrokinetic  
723 applications. *Current, Waves and Turbulence Measurement (CWTM), 2015 IEEE/OES Eleventh,*  
724 1–8, doi:10.1109/CWTM.2015.7098119.
- 725 Voulgaris, G., and J. H. Trowbridge, 1998: Evaluation of the acoustic doppler velocimeter (adv)  
726 for turbulence measurements. *Journal of Atmospheric and Oceanic technology*, **15**, 272–289.
- 727 Walter, R. K., N. J. Nidzieko, and S. G. Monismith, 2011: Similarity scaling of turbulence spectra  
728 and cospectra in a shallow tidal flow. *Journal of Geophysical Research: Oceans*, **116 (C10)**.
- 729 Warner, S. J., P. MacCready, J. N. Moum, and J. D. Nash, 2013: Measurement of tidal form drag  
730 using seafloor pressure sensors. *Journal of Physical Oceanography*, **43 (6)**, 1150–1172.
- 731 Wiles, P. J., T. P. Rippeth, J. H. Simpson, and P. J. Hendricks, 2006: A novel technique for  
732 measuring the rate of turbulent dissipation in the marine environment. *Geophysical Research  
733 Letters*, **33**, 21 608.
- 734 Winkel, D., M. Gregg, and T. Sanford, 1996: Resolving oceanic shear and velocity with the multi-  
735 scale profiler. *Journal of Atmospheric and Oceanic Technology*, **13 (5)**, 1046–1072.
- 736 Wyngaard, J. C., L. Rockwell, and C. A. Friehe, 1985: Errors in the measurement of turbulence  
737 upstream of an axisymmetric body. *Journal of Atmospheric and Oceanic Technology*, **2 (4)**,  
738 605–614.

<sup>739</sup> Zhang, Y., K. Streitlien, J. G. Bellingham, and A. B. Baggeroer, 2001: Acoustic doppler ve-  
<sup>740</sup> locimeter flow measurement from an autonomous underwater vehicle with applications to deep  
<sup>741</sup> ocean convection. *Journal of Atmospheric and Oceanic Technology*, **18** (12), 2038–2051, doi:  
<sup>742</sup> 10.1175/1520-0426(2001)018<2038:ADVFMF>2.0.CO;2.

## LIST OF FIGURES

743	<b>Fig. 1.</b>	Bathymetry of Admiralty Inlet near Port Townsend, Washington, U.S.A. (Finlayson 2005). The red dot indicates the location of all measurements. The positive $u$ direction is the direction of ebb flow (thick arrow originating from red dot), and positive $v$ is away from Admiralty Head (smaller arrow).	38
748	<b>Fig. 2.</b>	Schematic diagram of the TTM; not to scale.	39
749	<b>Fig. 3.</b>	TTM components on the deck of the R/V Jack Robertson. The TTM includes two ADVs, with pressure cases mounted on opposite sides of the fin. The anchor stack includes a pop-up buoy for retrieval. The green arrow indicates the vector from the IMU to the ADV head (face of the transmit transducer).	40
753	<b>Fig. 4.</b>	Top: Alex DeKlerk checks to ensure that the StableMoor buoy is properly fastened to its anchor; the RDI workhorse ADCP can be seen in the rear instrument bay. A bridle is draped across the top of the buoy for deployment and recovery, and a small marker buoy fastened to the tail is useful during recovery. Bottom: a close-up of the StableMoor <u>buoy</u> with the ADV head and the top of its pressure case. The green arrow indicates the vector from the IMU to the ADV head.	41
759	<b>Fig. 5.</b>	The turbulence platform showing details of the ADV head and pressure case configuration. The green arrow indicates the vector from the IMU to the ADV head. The head cable was taped out of the way beneath the sounding weight tail fins shortly after taking this photo.	42
762	<b>Fig. 6.</b>	The spectral noise levels of rotational velocity ( $S\{\vec{n}_\omega\}$ , yellow) and translational velocity ( $S\{\vec{n}_a\}$ , black) estimated from an ADV-IMU resting motionless on a table. Solid and dashed lines indicate the horizontal and vertical components, respectively, of $S\{\vec{n}_a\}$ and $S\{\vec{u}_{low}\}$ . The horizontal components are equivalent, as are all three components of $S\{\vec{n}_\omega\}$ . The $\vec{n}_a$ signals are unfiltered (black), and high-pass filtered at 30 s (purple) and 5 s (green); vertical dotted lines indicate the filter frequency. Blue lines are an estimate of $\vec{u}_{low}$ for the TTM. The horizontal and vertical Doppler noise levels of a Nortek Vector ADV configured to measure $\pm 4$ m/s are indicated by horizontal dash-dot and dotted lines, respectively. The shaded region indicates the range of $u$ spectral amplitudes presented herein ( $0.002 < \text{tke} < 0.03 \text{ m}^2/\text{s}^2$ , $1\text{e}-5 < \varepsilon < 5\text{e}-4 \text{ W/kg}$ ).	43
772	<b>Fig. 7.</b>	Motion-corrected velocity spectra, $S\{\vec{u}\}$ , for a range of high-pass filter frequencies: $f_a = 0.33$ Hz (red), 0.033 Hz (thick black), and 0.0033 Hz (cyan). The vertical dashed lines indicate the filter frequency. The thick grey line is $S\{\vec{u}_h\}$ for $f_a = 0.0033$ Hz. The data are from the June 2014 TTM deployment when $2.0 <  \vec{u}  < 2.5 \text{ ms}^{-1}$ .	44
776	<b>Fig. 8.</b>	Time series of tidal velocity at Admiralty Head from <u>TTM-ADV-IMU</u> measurements (black), and an acoustic Doppler profiler <u>on the anchor</u> (red). The profiler measurements—taken at the same depth as the ADV on the TTM—were contaminated by acoustic reflection from the strongback fin when it was inline with one of the profiler’s beams. Note that the vertical scale on the three axes vary by more than an order of magnitude; the small ticks in A and B are equivalent to the ticks in C.	45
782	<b>Fig. 9.</b>	Turbulence spectra from the June 2014 TTM deployment. Each column is for a range of streamwise velocity magnitudes (indicated at top). The rows are for each component of velocity (indicated to the lower right of the right column). The uncorrected spectra are in black and the corrected spectra are blue, and the spectra of ADV head motion, $\vec{u}_h$ , is red (also indicated in the legend). The vertical red dotted line indicates the filter frequency applied	

787 to the IMU accelerometers when estimating  $\vec{u}_h$ ; below this frequency  $S\{\vec{u}_h\}$  is plotted as a  
 788 dashed line. Diagonal black dotted lines indicate a  $f^{-5/3}$  slope. The number of spectral  
 789 ensembles, N, in each column is indicated in the top row. . . . .

46

790 **Fig. 10.** Turbulence spectra from the StableMoor buoy. The axes layout and annotations are identical  
 791 to Figure 9, except that  $S\{\vec{u}_h\}$  is plotted as a solid line at all frequencies because it is  
 792 measured at all frequencies. . . . .

47

793 **Fig. 11.** Turbulence spectra from the turbulence torpedo during a 35-minute period when the mean  
 794 velocity was 1.3 m/s. Annotations and line colors are identical to Figure 9. . . . .

48

795 **Fig. 12.** ~~The real part of the cross-spectral density~~ Variance preserving cross-spectra between  
 796 ~~velocity components measured by of~~  $\vec{u}$  (blue),  $\vec{u}_h$  (red), and  $\vec{u}_m$  (black) from the June 2014  
 797 TTM deployment. The upper row is ~~the  $u \cdot v$  cross-spectral density~~  $f \cdot C\{u, v\}$ , the middle row is ~~the  $u \cdot w$  cross-spectral density~~  $f \cdot C\{u, w\}$ , and the bottom row is ~~the  $v \cdot w$  cross-spectral density~~  $f \cdot C\{v, w\}$ . Note that these cross-spectra are between components of a velocity  
 800 vector (e.g.,  $\vec{u}$ ), not between different vectors (i.e., not between  $\vec{u}$  and  $\vec{u}_m$ ). The columns  
 801 are for different ensemble-averages over distinct ranges of the stream-wise mean velocity  
 802 magnitude (indicated above the top row). ~~The blue line~~  $N$  is the cross spectrum between  
 803 components ~~number of motion-corrected velocity, the red line is the cross spectrum between~~  
 804 components of head-motion, and the black line is the cross spectrum between components  
 805 of uncorrected velocity spectral ensembles in each column. The light blue shading indicates  
 806 one standard deviation of the  $C$  for the motion-corrected cross-spectral density  $f \cdot C\{\vec{u}\}$ .  $N$  is  
 807 the number of spectral ensembles in each column. The number in the lower-right corner of  
 808 each panel ~~is~~ indicates the motion-corrected ensemble-averaged estimate of the Reynold's  
 809 stress component (integral of the blue line) in units of  $10^{-4} \text{ m}^2 \text{s}^{-2}$   $10^{-3} \text{ m}^2 \text{s}^{-2}$ . . . . .

49

810 **Fig. 13.** Time series of mean velocities (A), turbulence energy and its components (B), Reynold's  
 811 stresses (C), and turbulence dissipation rate (D) measured by the TTM during the June  
 812 2014 deployment. Shading indicates periods of ebb ( $\bar{u} > 1.0 \text{ ms}^{-1}$ , grey) and flood  
 813 ( $\bar{u} < -1.0 \text{ ms}^{-1}$ , lighter grey). . . . .

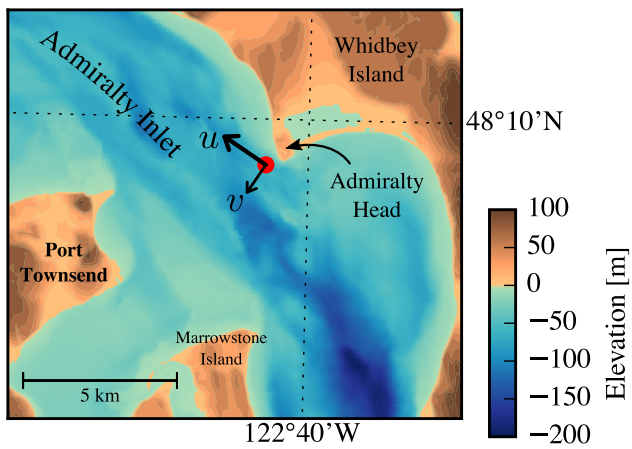
50

814 **Fig. 14.**  $P_{uz}$  vs.  $\epsilon$  during the June 2014 TTM deployment for values of  $|u| > 1 \text{ m/s}$ . Values of negative  
 815 production are indicated as open circles. . . . .

51

816 **Fig. 15.** A log-log plot of  $\epsilon$  versus  $\bar{U}$  for the June 2014 TTM (diamonds) and May 2015 StableMoor (dots) deployments, during ebb (left) and flood (right). Black points are 5-minute  
 817 averages. Green dots are mean values within speed bins of  $0.2 \text{ m s}^{-1}$  width that have at least  
 818 10 points (50 minutes of data); their vertical bars are 95% bootstrap confidence intervals.  
 819 The blue line shows a  $U^3$  slope, wherein the proportionality constant (blue box) is calculated  
 820 by taking the log-space mean of  $\epsilon/U^3$ . . . . .

52



822 FIG. 1. Bathymetry of Admiralty Inlet near Port Townsend, Washington, U.S.A. (Finlayson 2005). The red  
 823 dot indicates the location of all measurements. The positive  $u$  direction is the direction of ebb flow (thick arrow  
 824 originating from red dot), and positive  $v$  is away from Admiralty Head (smaller arrow).

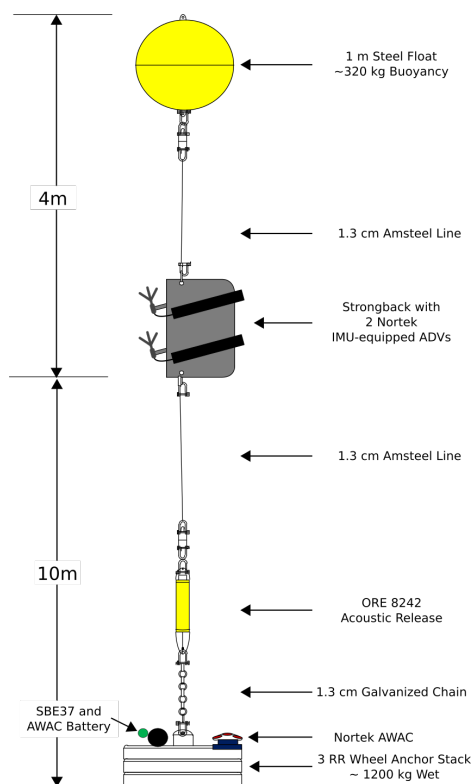
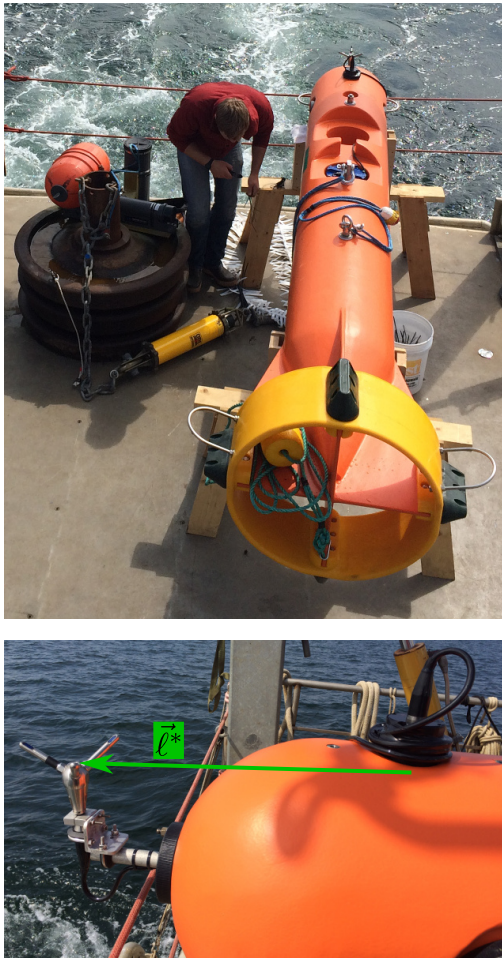


FIG. 2. Schematic diagram of the TTM; not to scale.



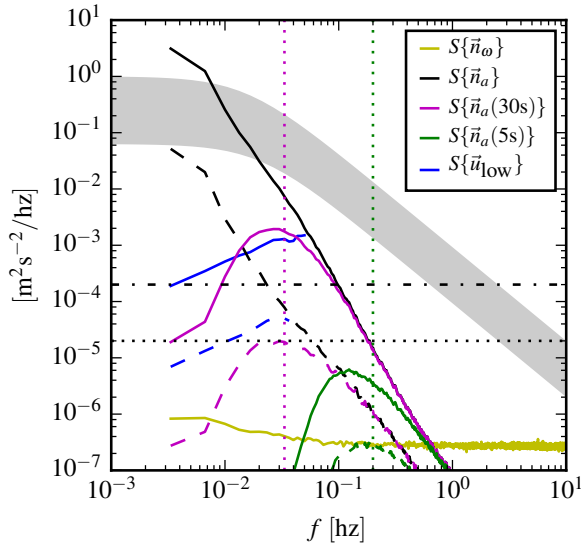
825 FIG. 3. TTM components on the deck of the R/V Jack Robertson. The TTM includes two ADVs, with  
826 pressure cases mounted on opposite sides of the fin. The anchor stack includes a pop-up buoy for retrieval. The  
827 green arrow indicates the vector from the IMU to the ADV head (face of the transmit transducer).



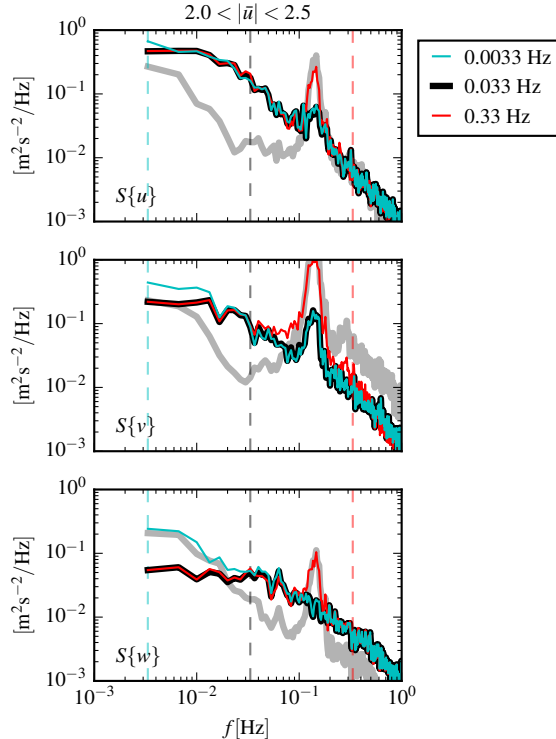
828 FIG. 4. Top: Alex DeKlerk checks to ensure that the StableMoor buoy is properly fastened to its anchor; the  
 829 RDI workhorse ADCP can be seen in the rear instrument bay. A bridle is draped across the top of the buoy  
 830 for deployment and recovery, and a small marker buoy fastened to the tail is useful during recovery. Bottom: a  
 831 close-up of the StableMoor buoy with the ADV head and the top of its pressure case. The green arrow indicates  
 832 the vector from the IMU to the ADV head.



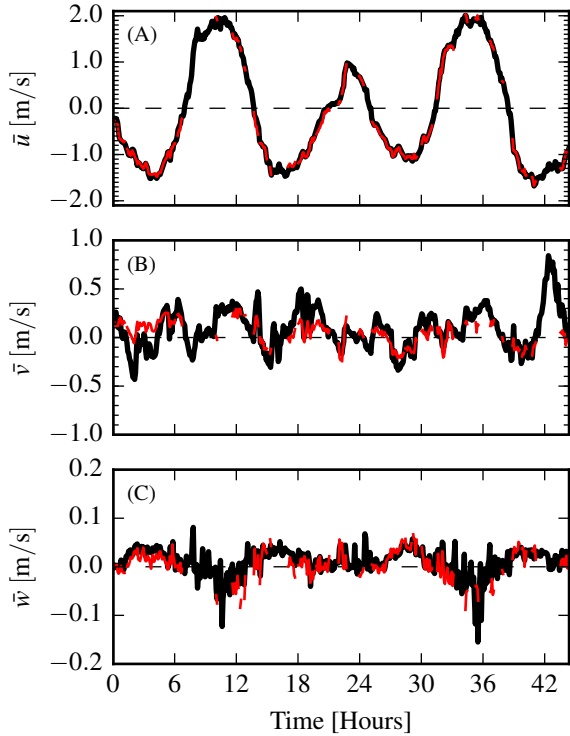
833 FIG. 5. The turbulence platform showing details of the ADV head and pressure case configuration. The green  
834 arrow indicates the vector from the IMU to the ADV head. The head cable was taped out of the way beneath the  
835 sounding weight tail fins shortly after taking this photo.



836 FIG. 6. The spectral noise levels of rotational velocity ( $S\{\vec{n}_\omega\}$ , yellow) and translational velocity ( $S\{\vec{n}_a\}$ ,  
 837 black) estimated from an ADV-IMU resting motionless on a table. Solid and dashed lines indicate the horizontal  
 838 and vertical components, respectively, of  $S\{\vec{n}_a\}$  and  $S\{\vec{u}_{low}\}$ . The horizontal components are equivalent, as are  
 839 all three components of  $S\{\vec{n}_\omega\}$ . The  $\vec{n}_a$  signals are unfiltered (black), and high-pass filtered at 30 s (purple)  
 840 and 5 s (green); vertical dotted lines indicate the filter frequency. Blue lines are an estimate of  $\vec{u}_{low}$  for the  
 841 TTM. The horizontal and vertical Doppler noise levels of a Nortek Vector ADV configured to measure  $\pm 4 \text{ m/s}$   
 842 are indicated by horizontal dash-dot and dotted lines, respectively. The shaded region indicates the range of  $u$   
 843 spectral amplitudes presented herein ( $0.002 < \text{tke} < 0.03 \text{ m}^2/\text{s}^2$ ,  $1\text{e}-5 < \epsilon < 5\text{e}-4 \text{ W/kg}$ ).



844 FIG. 7. Motion-corrected velocity spectra,  $S\{\vec{u}\}$ , for a range of high-pass filter frequencies:  $f_a = 0.33$  Hz  
 845 (red), 0.033 Hz (thick black), and 0.0033 Hz (cyan). The vertical dashed lines indicate the filter frequency.  
 846 The thick grey line is  $S\{\vec{u}_h\}$  for  $f_a = 0.0033$  Hz. The data are from the June 2014 TTM deployment when  
 847  $2.0 < |\vec{u}| < 2.5 \text{ ms}^{-1}$ .



848 FIG. 8. Time series of tidal velocity at Admiralty Head from TTM-ADV-IMU measurements (black), and an  
 849 acoustic Doppler profiler on the anchor (red). The profiler measurements—taken at the same depth as the ADV  
 850 on the TTM—were contaminated by acoustic reflection from the strongback fin when it was inline with one of  
 851 the profiler’s beams. Note that the vertical scale on the three axes vary by more than an order of magnitude; the  
 852 small ticks in A and B are equivalent to the ticks in C.

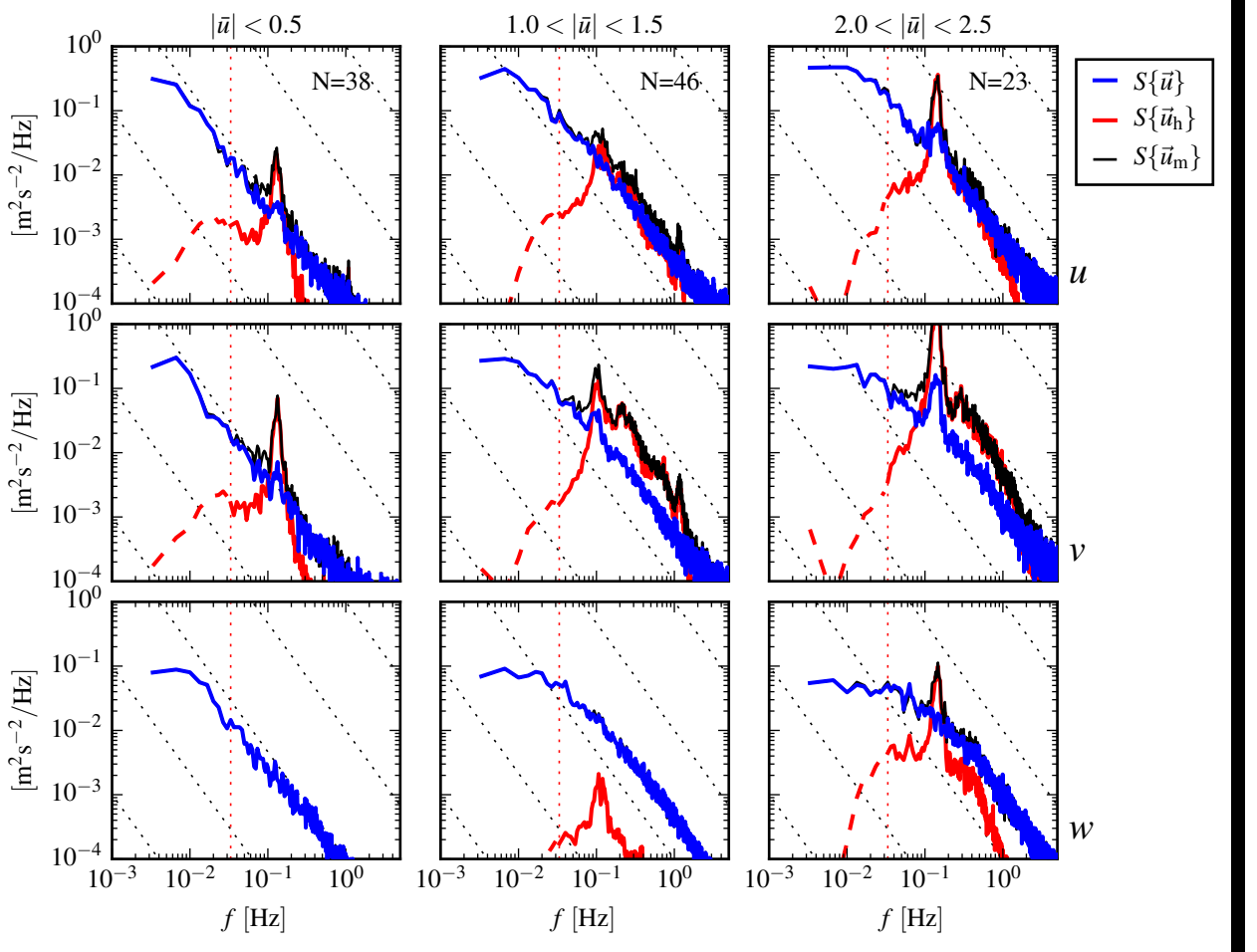
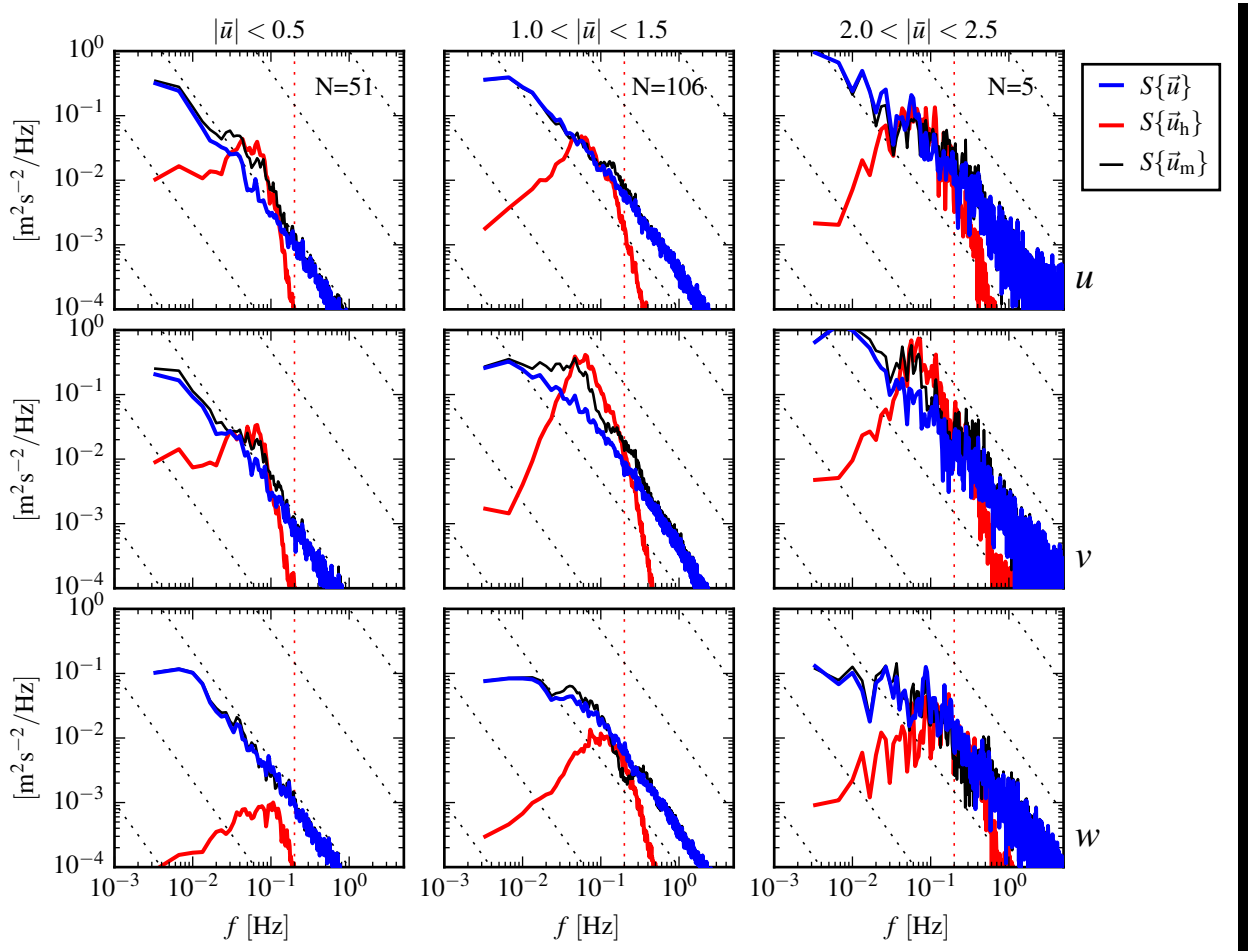
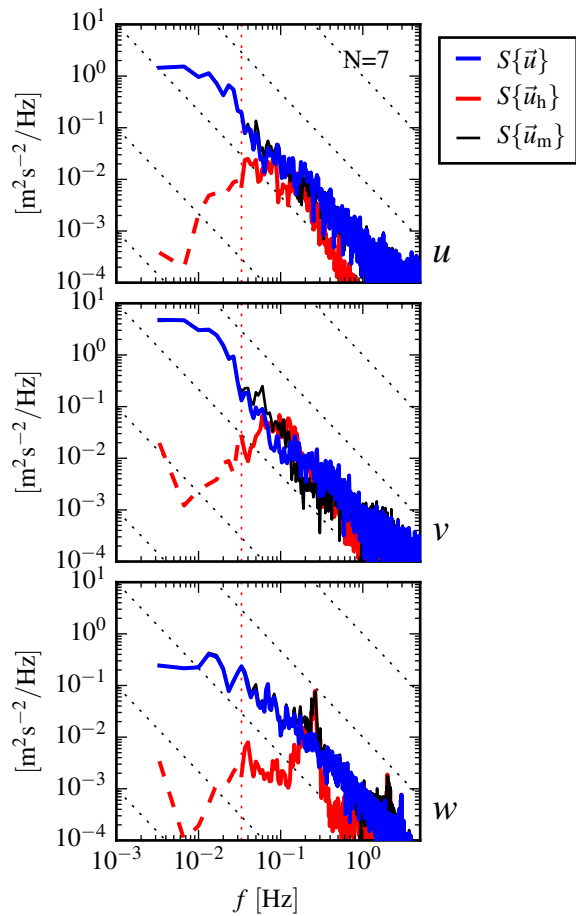


FIG. 9. Turbulence spectra from the June 2014 TTM deployment. Each column is for a range of streamwise velocity magnitudes (indicated at top). The rows are for each component of velocity (indicated to the lower right of the right column). The uncorrected spectra are in black and the corrected spectra are blue, and the spectra of ADV head motion,  $\vec{u}_h$ , is red (also indicated in the legend). The vertical red dotted line indicates the filter frequency applied to the IMU accelerometers when estimating  $\vec{u}_h$ ; below this frequency  $S\{\vec{u}_h\}$  is plotted as a dashed line. Diagonal black dotted lines indicate a  $f^{-5/3}$  slope. The number of spectral ensembles,  $N$ , in each column is indicated in the top row.



860 FIG. 10. Turbulence spectra from the StableMoor buoy. The axes layout and annotations are identical to  
 861 Figure 9, except that  $S\{\vec{u}_h\}$  is plotted as a solid line at all frequencies.



862 FIG. 11. Turbulence spectra from the turbulence torpedo during a 35-minute period when the mean velocity  
 863 was 1.3 m/s. Annotations and line colors are identical to Figure 9.

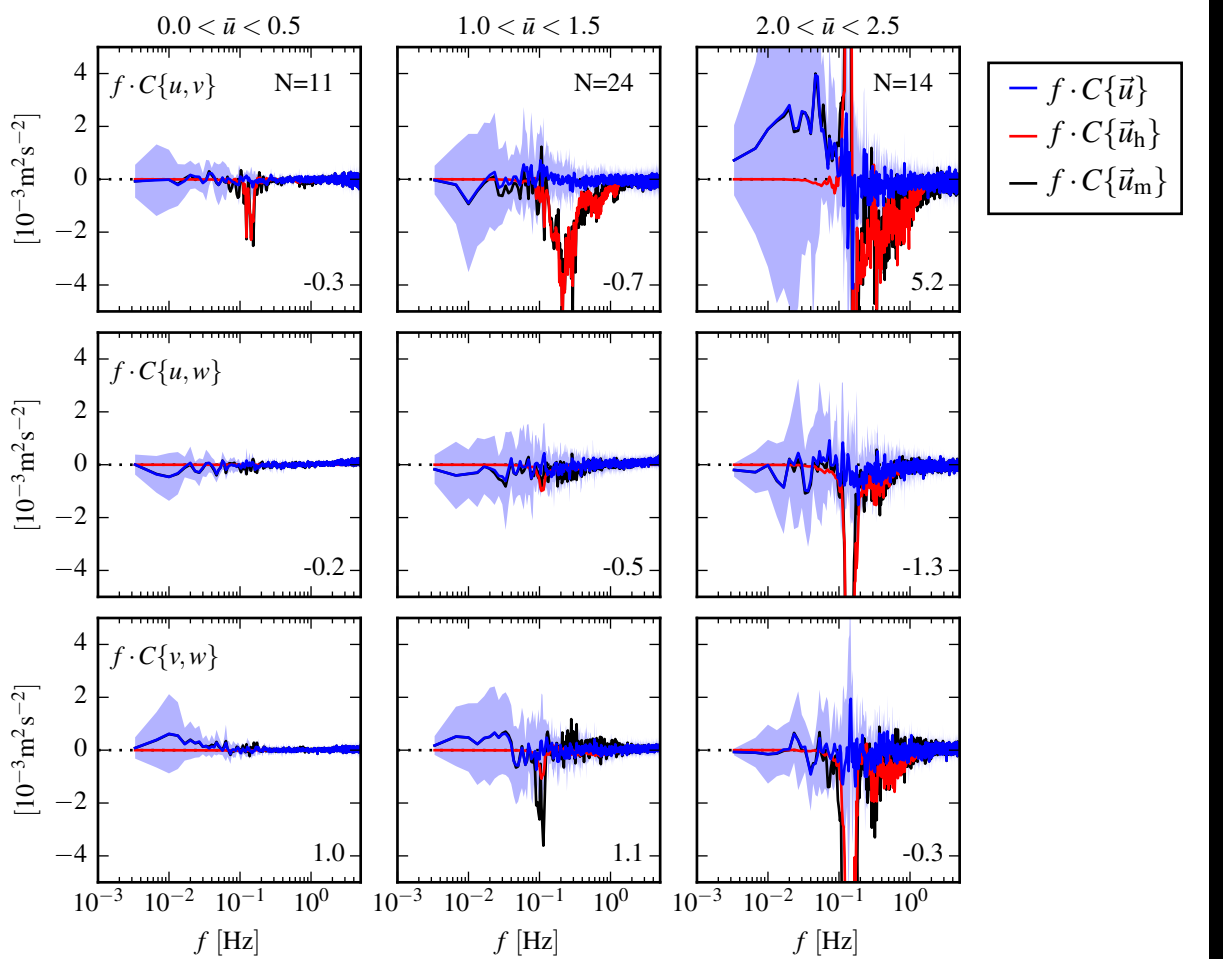


FIG. 12. The real part of the cross-spectral density Variance preserving cross-spectra between velocity components measured by of  $\vec{u}$  (blue),  $\vec{u}_h$  (red), and  $\vec{u}_m$  (black) from the June 2014 TTM deployment. The upper row is the  $u \cdot v$  cross-spectral density  $f \cdot C\{u, v\}$ , the middle row is the  $u \cdot w$  cross-spectral density  $f \cdot C\{u, w\}$ , and the bottom row is the  $v \cdot w$  cross-spectral density  $f \cdot C\{v, w\}$ . Note that these cross-spectra are between components of a velocity vector (e.g.,  $\vec{u}$ ), not between different vectors (i.e., not between  $\vec{u}$  and  $\vec{u}_m$ ). The columns are for different ensemble-averages over distinct ranges of the stream-wise mean velocity magnitude (indicated above the top row). The blue line  $N$  is the cross-spectrum between components number of motion-corrected velocity, the red line is the cross spectrum between components of head-motion, and the black line is the cross spectrum between components of uncorrected velocity spectral ensembles in each column. The light blue shading indicates one standard deviation of the  $C$  for the motion-corrected cross-spectral density  $f \cdot C\{\vec{u}\}$ .  $N$  is the number of spectral ensembles in each column. The number in the lower-right corner of each panel is indicates the motion-corrected ensemble-averaged estimate of the Reynold's stress component (integral of the blue line) in units of  $10^{-4} \text{ m}^2 \text{s}^{-2}$ .

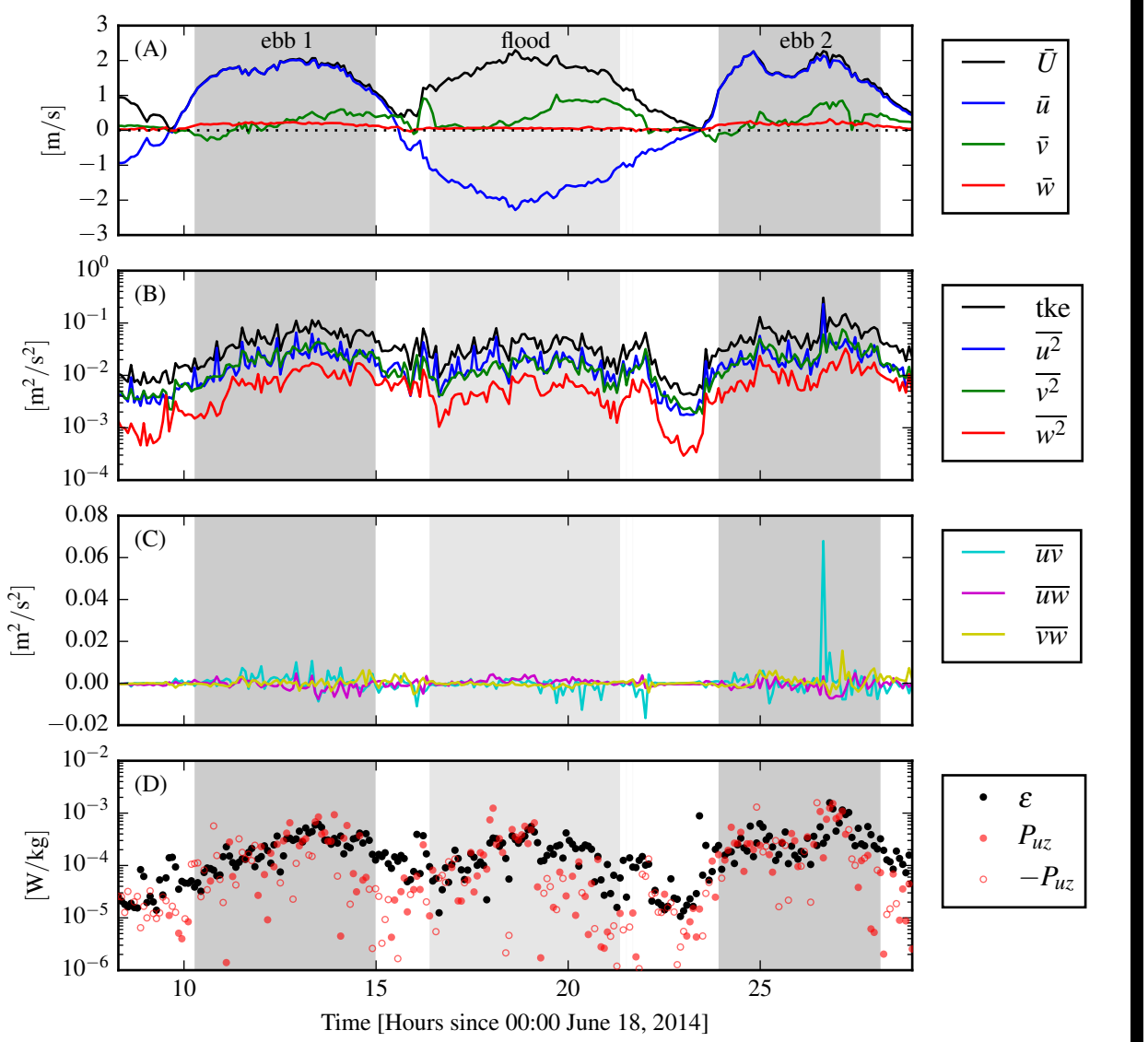
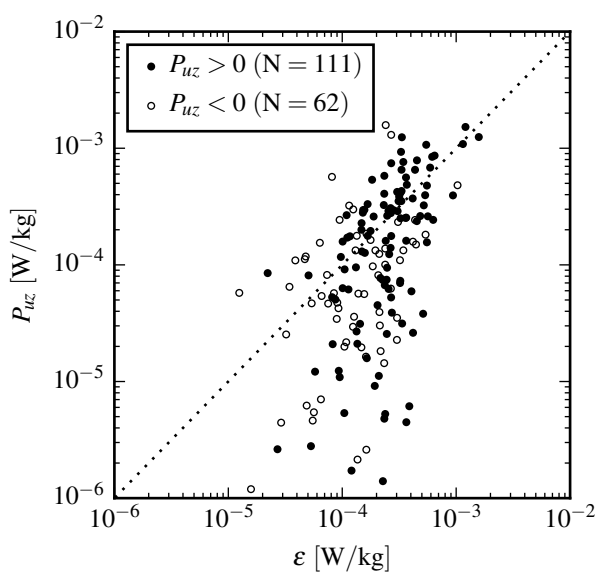


FIG. 13. Time series of mean velocities (A), turbulence energy and its components (B), Reynold's stresses (C), and turbulence dissipation rate (D) measured by the TTM during the June 2014 deployment. Shading indicates periods of ebb ( $\bar{u} > 1.0 \text{ ms}^{-1}$ , grey) and flood ( $\bar{u} < -1.0 \text{ ms}^{-1}$ , lighter grey).



880 FIG. 14.  $P_{uz}$  vs.  $\epsilon$  during the June 2014 TTM deployment for values of  $|u| > 1$  m/s. Values of negative  
881 production are indicated as open circles.

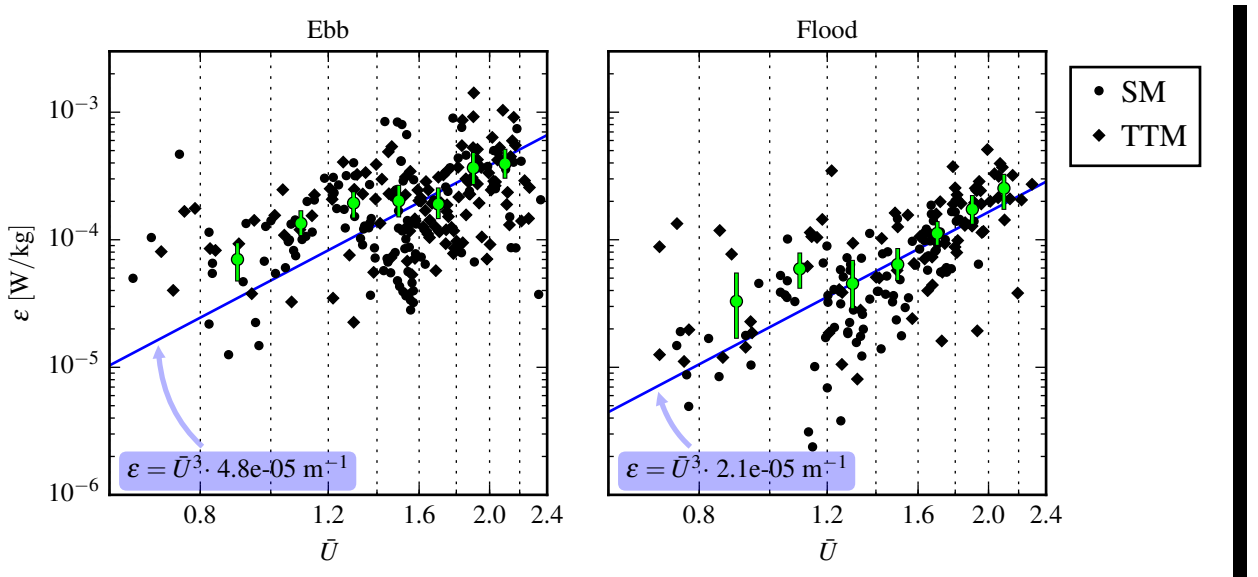


FIG. 15. A log-log plot of  $\varepsilon$  ~~versus~~-vs.  $\bar{U}$  for the June 2014 TTM (diamonds) and May 2015 StableMoor (dots) deployments, during ebb (left) and flood (right). Black points are 5-minute averages. Green dots are mean values within speed bins of  $0.2 \text{ m s}^{-1}$  width that have at least 10 points (50 minutes of data); their vertical bars are 95% bootstrap confidence intervals. The blue line shows a  $U^3$  slope, wherein the proportionality constant (blue box) is calculated by taking the log-space mean of  $\varepsilon/U^3$ .